Quantifying Intrinsic and Extrinsic Contributions to Radial Anisotropy in Tomographic Models

J K Magali, T Bodin, N Hedjazian, Y. Ricard, Y Capdeville, E Debayle

JGR Solid Earth

RESEARCH ARTICLE
10.1029/2021JB022322

Quantifying Intrinsic and Extrinsic Contributions to Radial Anisotropy in Tomographic Models

J. K. Magali[1], T. Bodin[1], N. Hedjazian[1], Y. Ricard[1], Y. Capdeville[2], and E. Debayle[1]

[1]Univ Lyon, UCBL, ENSL, UJM, CNRS, LGL-TPE, Villeurbanne, France, [2]Laboratoire de Planétologie et Géodynamique, CNRS, UMR 6112, Université de Nantes, Nantes, France

Key Points:

- We propose a theoretical expression that relates the observed radial anisotropy to its intrinsic and extrinsic contributions
- At wavelengths longer than the scale of deformation patterns, tomography underestimates intrinsic anisotropy due to spatial averaging
- At shorter wavelengths, tomography overestimates intrinsic anisotropy due to the presence of extrinsic anisotropy

Correspondence to:
J. K. Magali,
jkvmagali@gmail.com

Citation:
Magali, J. K., Bodin, T., Hedjazian, N., Ricard, Y., Capdeville, Y., & Debayle, E. (2021). Quantifying intrinsic and extrinsic contributions to radial anisotropy in tomographic models. *Journal of Geophysical Research: Solid Earth*, *126*, e2021JB022322. https://doi.org/10.1029/2021JB022322

Received 28 APR 2021
Accepted 30 SEP 2021

Abstract Seismic anisotropy in the Earth's mantle inferred from seismic observations is usually interpreted in terms of intrinsic anisotropy due to crystallographic preferred orientation (CPO) of minerals, or extrinsic anisotropy due to shape preferred orientation (SPO). The coexistence of both contributions confuses the origins of seismic anisotropy observed in tomographic models. It is thus essential to discriminate CPO from SPO. Homogenization/upscaling theory provides means to achieve this goal. It enables computing the effective elastic properties of a heterogeneous medium, as seen by long-period waves. In this work, we investigate the effects of upscaling an intrinsically anisotropic and heterogeneous mantle. We show analytically in 1-D that the observed radial anisotropy parameter ξ^* is approximately the product of the intrinsic ξ^*_{CPO} and the extrinsic ξ^*_{SPO} components: $\xi^* \approx \xi^*_{\mathrm{CPO}} \times \xi^*_{\mathrm{SPO}}$. This law is verified numerically in the case of a homogenized 2-D marble cake model of the mantle in the presence of CPO obtained from a micro-mechanical model of olivine deformation. Our numerical findings predict that for wavelengths smaller than the scale of deformation patterns, tomography may overestimate intrinsic anisotropy due to significant extrinsic anisotropy. At longer wavelengths, intrinsic anisotropy is always underestimated due to spatial averaging. Therefore, we show that it is imperative to homogenize a CPO model first before drawing comparisons with tomographic models. As a demonstration, we use our composite law with a homogenized CPO model of a plate-driven flow underneath a mid-ocean ridge, to estimate the SPO contribution to an existing tomographic model of radial anisotropy.

Plain Language Summary Small-scale heterogeneities may generate long-period seismic observations that are identical to those produced by large-scale mantle flow and deformation. Because of this, it is difficult to distinguish in the observed seismic anisotropy what is related to the intrinsic crystalline anisotropy and what may be due to the laminated structure of isotropic materials. In this study, we undertook an analytical method and a numerical experiment to identify the separate effects of intrinsic and apparent anisotropy in a long wave-length tomographic image. We show that the ambiguity depends on the relation between the wavelength of the observed wavefield and the scale of convection patterns in the mantle. This motivated us to develop a simple composite law that can be used to quantify the two separate contributions.

1. Introduction

Seismic anisotropy in the Earth's mantle originates from various processes and can be observed at different spatial scales (Hansen et al., 2021; Kendall, 2000). At the mineral scale, crystallographic preferred orientation (CPO), also sometimes called lattice preferred orientation (LPO), of anisotropic mantle minerals due to progressive shearing over time produces large-scale intrinsic anisotropy (Maupin & Park, 2015; Nicolas & Christensen, 1987). On the other hand, rock-scale shape preferred orientation (SPO) such as layered heterogeneous materials, seismic discontinuities, preferentially oriented cracks, or conduits containing fluid intrusions unresolved by long-period seismic waves are mapped as large-scale extrinsic anisotropy (Backus, 1962; Crampin & Booth, 1985).

Although these two mechanisms are completely different, a medium may be either (or both) intrinsically anisotropic and extrinsically anisotropic at a given scale, depending on the minimum wavelength of the observed wavefield used (Bodin et al., 2015; Fichtner et al., 2013; Maupin et al., 2007; Wang et al., 2013). Backus (1962) showed that a horizontally layered isotropic medium is equivalent to a homogeneous radially anisotropic medium with a vertical axis of symmetry when sampled by seismic waves whose wavelength is

much longer than the thickness of layers. This urged seismologists to interpret tomographic models separately depending on the type of data used (i.e., different data types sample different length scales). Scattering studies use high-frequency body waves and interpret small-scale isotropic heterogeneities in terms of phase changes (e.g., Tauzin & Ricard, 2014) or chemical stratification (e.g., Tauzin et al., 2016). On the other hand, long-period surface waves with typical wavelengths of the order 10^2 km retrieve a smooth anisotropic mantle with scales consistent with convective flow (e.g., Beghein et al., 2010; Bodin et al., 2015; Debayle & Ricard, 2013; Maupin & Park, 2015). Surface waves however lack the resolving power to recover sharp seismic discontinuities and instead, map these as long-wavelength radial anisotropy (Backus, 1962; Capdeville et al., 2013). The ambiguity on the origin of observed anisotropy (i.e., whether a material is intrinsically anisotropic or strongly heterogeneous) may mislead seismologists in interpreting the structural origin of seismic anisotropy observed in tomographic images.

1.1. Intrinsic Anisotropy Due to Crystallographic Preferred Orientation

Intrinsic anisotropy results from the preferred alignment of anisotropic crystals in an aggregate when subjected to a macroscopic deformation. In the mantle, single-crystal olivine exhibits orthorhombicity, and hence suffers variations in fast and slow P-wave and S-wave velocities up to 20 % (Kumazawa & Anderson, 1969). When olivine and pyroxene form a polycrystalline aggregate and are subsequently deformed in the mantle flow, their CPO can be described at first order in terms of a hexagonally symmetric medium (e.g., Montagner & Nataf, 1988).

Observations of large-scale anisotropy in tomographic models appear to be ubiquitous in regions associated with strong deformation, and have often been interpreted in terms of convective flow (Long, 2013; McKenzie, 1979). For instance, tomographic imaging has revealed the presence of strong azimuthal and radial anisotropy in the upper ~250 km of the mantle (refer to Long and Becker [2010] for a comprehensive review). Long-wavelength seismic anisotropy is also prevalent in the transition zone (e.g., Trampert & van Heijst, 2002; Wookey & Kendall, 2004) although its origin is still highly debated (Chang & Ferreira, 2019; Chen & Brudzinski, 2003; Sturgeon et al., 2019). Probing deeper depths, the lower mantle appears to be isotropic (e.g., Meade et al., 1995) barring the D" layer where enough evidence have shown it to be anisotropic (e.g., Beghein et al., 2006; Kendall & Silver, 1998; McNamara et al., 2002; Panning & Romanowicz, 2006).

Since CPO maps the deformation patterns, CPO may deviate from the flow direction. This is because the deformation patterns relate not to the velocity field itself, but to the velocity gradient. Moreover, CPO is not instantaneous, but depends on the history of the deformation. As a result, regions with short deformation trajectories such as beneath mid-ocean ridges appear to have under-developed CPO, and would lag behind the direction of shear deformation (Kaminski & Ribe, 2002).

Based on laboratory experiments of simple shear, the fast axis of olivine tends to align parallel to the long axis of the finite strain ellipsoid at low strains due to plastic deformation (Zhang & Karato, 1995). At larger strains, dynamic recrystallization facilitates the alignment of the olivine fast axis toward the direction of shear (Bystricky et al., 2000; Zhang & Karato, 1995). Mechanical models of CPO evolution, coupled with geodynamic flow modeling have been developed to replicate these results and have been extrapolated at scales consistent with mantle deformation patterns. Among these is the viscoplastic self-consistent model which is used to explain the mechanical response of polycrystals to plastic deformation (Tommasi et al., 2000). Such tools however are computationally expensive, especially when applied to 3-D and non-steady-state flows (Lev & Hager, 2008). Another well-received method is the D-Rex model, which utilizes a simple kinematic approach (Kaminski et al., 2004). The predicted CPO is then converted to an elastic medium in which seismic waves can propagate, and may explain anisotropic signatures observed in seismic data recorded at the surface.

1.2. Extrinsic Anisotropy Due to Shape Preferred Orientation

Extrinsic anisotropy is observed under two conditions: (a) when the scale of the heterogeneities is much smaller than the minimum wavelength of the observed wavefield, and (b) when the contrast between seismic wave velocities (i.e., the amplitude of heterogeneities) is large.

One of the known configurations at which extrinsic anisotropy produced is rock-scale SPO. In the Earth's mantle, rock-scale SPO can be the result of igneous differentiation, or more generally of the stirring of chemical heterogeneities by tectonic or convective deformation (e.g., Faccenda et al., 2019). Since magmatically differentiated oceanic lithosphere is composed of a basaltic crustal layer blanketed by a depleted harzburgitic mantle (Allègre & Turcotte, 1986), mantle structure is often modeled in terms of a mechanical mixture of these two end-member compositions (e.g., Ballmer et al., 2015; Hofmann, 1988; Xu et al., 2008).

Large-scale thermal convection in the mantle triggers the constant injection of oceanic lithosphere into the mantle (Coltice & Ricard, 1999). It then mechanically stirs with the surrounding mantle and experiences a series of stretching and thinning due to the normal and shear strains associated with convection (Allègre & Turcotte, 1986). This led Allègre and Turcotte (1986) to develop a geodynamic model of the mantle that would depict marble cake-like patterns. In their model, the layering may be erased either by dissolution processes when the stripes become thin enough that chemical diffusion becomes efficient, or by mantle reprocessing at mid-ocean ridges. Assuming that the mixing preserves the physical properties of the two-end members with depth and over geological time scales, such processes may explain rock-scale seismic heterogeneities observed in the mantle in agreement with the spectrum of isotropic anomalies observed along ridges (Agranier et al., 2005; Stixrude & Jeanloz, 2015; Xu et al., 2008).

1.3. Long-Period Tomography

There are a plethora of ways to extract interpretable information from seismic data. Tomographic imaging techniques however are limited by the type of data used due to both computational, and theoretical considerations. Long-period tomography uses the relatively low-frequency components of a seismogram such as low-frequency travel time residuals, surface wave data, and normal-mode spectral measurements (e.g., Masters et al., 1996; Resovsky & Ritzwoller, 1999) to image mantle structure. In practice, they are primarily used to invert for absolute V_S structures and S –wave anisotropy (e.g., French et al., 2013; Gung et al., 2003; Panning & Romanowicz, 2006), although some studies have already documented the use of similar techniques to reconstruct V_P structures (e.g., Koelemeijer et al., 2016; Masters et al., 2000).

In the context of inversion for radial anisotropy, long-period tomography fails to distinguish between an intrinsic or an extrinsic origin. For instance, some tomographic models of radial anisotropy inferred from surface wave inversions cannot be explained with mineralogical models alone. These profiles of radial anisotropy are instead partly interpreted as unmapped small-scales either due to fine-layering, or by sharp gradients of lateral heterogeneities (e.g., Debayle & Kennett, 2000; Friederich & Huang, 1996; Kawakatsu et al., 2009; Montagner & Jobert, 1988; Schlue & Knopoff, 1977).

Indeed, the scale of these heterogeneities is far smaller in comparison with the wavefield considered in long-period tomography, and for this reason, the small scales are being mapped as extrinsic anisotropy. Anisotropic structures retrieved from tomography may therefore be a combination of extrinsic anisotropy due to SPO and deformation-induced intrinsic anisotropy. However, separating the intrinsic and the extrinsic contributions to the observed anisotropy is much difficult in full generality. To simplify the problem, we will focus on quantifying the separate contributions to S –wave radial anisotropy. This follows most studies that explored the extrinsic contributions to radial anisotropy (Alder et al., 2017; Bodin et al., 2015; Fichtner et al., 2013; Wang et al., 2013). Furthermore, we will also ignore the contributions of P –wave anisotropy which are not well-constrained by long-period tomography, particularly in the upper-mantle which is mostly constrained by surface waves that have little sensitivity to P properties (Takeuchi & Saito, 1972).

In this study, we extend the work of Alder et al. (2017) by estimating the long-wavelength effective equivalent of a marble cake mantle as hypothesized by Allègre and Turcotte (1986), but in the presence of intrinsic anisotropy. Our aim is to quantify the level of effective radial anisotropy resulting from elastic homogenization, that is, the relegated version of the true Earth as seen by long-wavelength seismic tomography. Section 2 is a brief overview of the homogenization theory and provides a definition of some terms and notations to guide the reader throughout the study. Section 3 shows 1-D analytical expressions for homogenization and highlights a composite law that separates intrinsic and extrinsic radial anisotropy for a layered and anisotropic media. Here, we demonstrate that the effective radial anisotropy varies with the square of isotropic heterogeneities, as well as with the square of anisotropic heterogeneities, plus a cross term

related to their coupling. In Section 4, we build a 2-D media analogous to the marble cake model where we consider a mechanical mixture of two end-member compositions. We follow this by introducing intrinsic anisotropy due to mantle deformation associated with convection patterns consistent with the marble cake model. We compute the long-wavelength effective equivalent of the 2-D models using the Fast-Fourier Homogenization algorithm (Capdeville et al., 2015). Section 5 presents the results of the previous section: one of the major findings is that in the absence of isotropic heterogeneities, intrinsic anisotropy is always underestimated upon homogenization due to the spatial averaging of the preferred orientation of the anisotropic minerals. We also verify numerically that the composite law derived in Section 3 can be extended to 2-D media. Finally, in Section 6, we apply the composite law to infer the extrinsic component of radial anisotropy from a tomographic model of the upper-mantle beneath a mid-ocean ridge with the help of a homogenized CPO model.

2. Elastic Homogenization

Even assuming perfect data coverage, seismic tomography is only able to recover a smooth representation of the real Earth due to the limited frequency band of seismic data. This smooth average, however, is not just a simple spatial average but is produced from highly non-linear upscaling relations. In the context of wave propagation, such upscaling relations, also known as elastic homogenization, remove seismic heterogeneities whose scales are much smaller than the minimum wavelength of the observed wavefield, and instead replace them with effective properties.

Hereafter, what we refer to as the *true elastic structure* $\mathbf{S}(\mathbf{r})$ is an elastic model of the real Earth varying in space $\mathbf{r}$ that accounts for both intrinsic anisotropy due to CPO and small-scale isotropic heterogeneities that resemble marble cake-like patterns. One can express $\mathbf{S}(\mathbf{r})$ in terms of a spatially varying isotropic tensor $\mathbf{S_I}(\mathbf{r})$ defined by the two Lamé parameters: $\lambda(\mathbf{r})$ and $\mu(\mathbf{r})$, plus an intrinsically anisotropic component $\mathbf{S_A}(\mathbf{r})$ related to CPO:

$$\mathbf{S}(\mathbf{r}) = \mathbf{S_I}(\mathbf{r}) + \mathbf{S_A}(\mathbf{r}), \tag{1}$$

where $\mathbf{S_I}(\mathbf{r})$ can be decomposed further into:

$$\mathbf{S_I}(\mathbf{r}) = \mathbf{S_0} + \delta\mathbf{S_I}(\mathbf{r}). \tag{2}$$

Here, $\mathbf{S_0}$ is an isotropic tensor uniform in space, and $\delta\mathbf{S_I}(\mathbf{r})$ is a deviation from $\mathbf{S_0}$ related to small-scale isotropic heterogeneities. The true elastic structure becomes:

$$\mathbf{S}(\mathbf{r}) = \mathbf{S_0} + \delta\mathbf{S_I}(\mathbf{r}) + \mathbf{S_A}(\mathbf{r}). \tag{3}$$

For convenience, let us introduce an operator $\mathcal{I}$ that extracts the isotropic component from $\mathbf{S}$, and an operator $\mathcal{A}$ that extracts the anisotropic component from $\mathbf{S}$:

$$\begin{aligned} \mathcal{I}(\mathbf{S}(\mathbf{r})) &= \mathbf{S_I}(\mathbf{r}) = \mathbf{S_0} + \delta\mathbf{S_I}(\mathbf{r}) \\ \mathcal{A}(\mathbf{S}(\mathbf{r})) &= \mathbf{S_0} + \mathbf{S_A}(\mathbf{r}), \end{aligned} \tag{4}$$

where $\mathcal{I}$ extracts the isotropic component by first computing the dilatational and Voigt stiffness tensors followed by the computation of the bulk and the shear moduli (Cowin & Mehrabadi, 1987), and $\mathcal{A}$ performs similar to the elastic decomposition method of Browaeys and Chevrot (2004) where the anisotropic component is treated as a sum of orthogonal projections belonging to several symmetry classes.

These notations will be used heavily in the rest of the text to denote the isotropic and anisotropic components of an elastic medium. Radial anisotropy, in particular, quantifies the level of anisotropy when the medium is averaged azimuthally (Maupin et al., 2007; Montagner, 2007). In such a vertically transverse isotropic (VTI) medium, the level of S –wave radial anisotropy is given by the anisotropic parameter $\xi = (V_{SH}/V_{SV})^2$, where V_{SV} is the velocity of vertically traveling S –waves or horizontally traveling S –waves with vertical polarization, and V_{SH} is the velocity of horizontally traveling S –waves with horizontal polarization. The *intrinsic S –wave radial anisotropy* extracted from $\mathcal{A}(\mathbf{S})$ (i.e., due to the component $\mathbf{S_A}$) will be denoted by ξ_{CPO}.

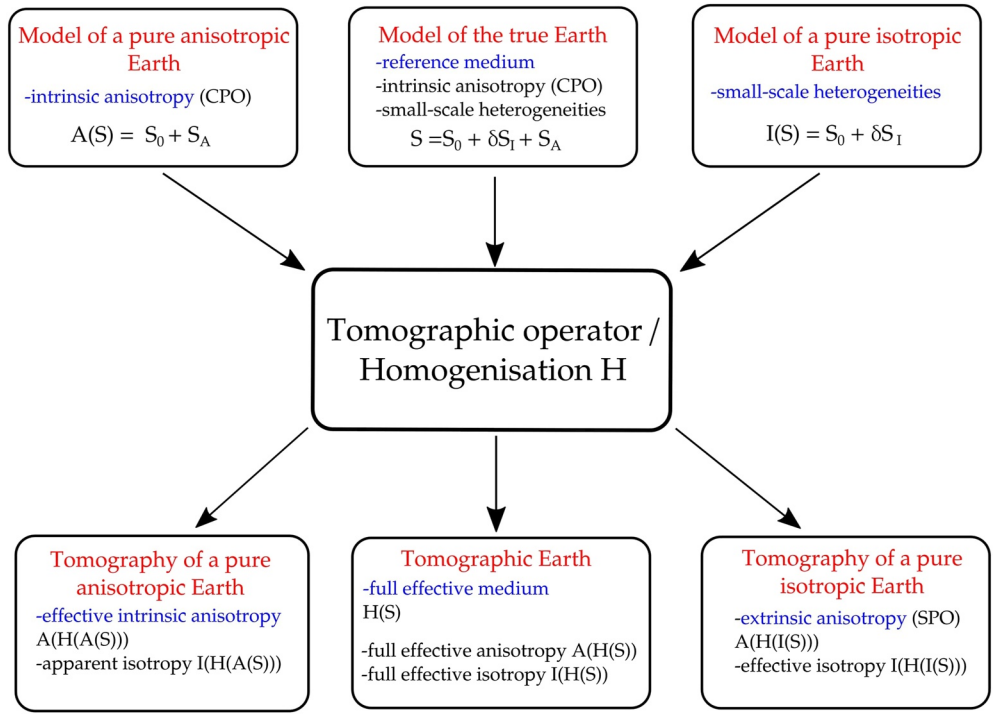

Figure 1. Homogenization of different Earth models and their respective outputs. The true Earth mantle (top middle box) is described by an average isotropic model $\mathbf{S_0}$, isotropic heterogeneities, $\delta\mathbf{S_I}$, and intrinsic anisotropy $\mathbf{S_A}$, the sum of which being the elastic model $\mathbf{S}$ that tomography tries to recover. However, tomographic methods have only access to a homogenized model $\mathcal{H}(\mathbf{S})$ (or full effective medium). This model has both isotropic components symbolized by $\mathcal{I}(\mathcal{H}(\mathbf{S}))$ and anisotropic components, $\mathcal{A}(\mathcal{H}(\mathbf{S}))$. The goal of this study is to quantify the differences between $\mathcal{A}(\mathcal{H}(\mathbf{S}))$ and $\mathcal{A}(\mathbf{S})$, $\mathcal{I}(\mathcal{H}(\mathbf{S}))$ and $\mathcal{I}(\mathbf{S})$. Numerically we can also discuss how an anisotropic model without isotropic heterogeneities (boxes on the left) can be recovered and if the tomographic inversion can lead to apparent isotropic heterogeneities. Reciprocally (boxes on the right), one can quantify how much a pure isotropic model is recovered by the tomographic inversion and what is the level of extrinsic anisotropy (SPO) that can be estimated.

In the event where long-period waves sample the true elastic structure, small-scale heterogeneities are seen only through their effective properties. Computing these effective properties is designated by a mathematical operator $\mathcal{H}$ called *upscaling* or *homogenization*. Setting aside the imperfections of inversion algorithms and data coverage, performing seismic tomography can be viewed as applying the operator that homogenizes $\mathbf{S}$. The seismic tomography model/long-wavelength effective medium of $\mathbf{S}$ is then $\mathcal{H}(\mathbf{S}) = \mathcal{H}(\mathbf{S_0} + \delta\mathbf{S_I} + \mathbf{S_A})$ which we now refer to as the *full effective medium*. The anisotropic component of the full effective medium given by $\mathcal{A}(\mathcal{H}(\mathbf{S}))$ will be referred hereafter as the *full effective anisotropy* and its isotropic component $\mathcal{I}(\mathcal{H}(\mathbf{S}))$ is the *full effective isotropy*. We will symbolize the *full effective radial anisotropy* corresponding to $\mathcal{A}(\mathcal{H}(\mathbf{S}))$ with ξ^*.

On the other hand, the homogenized counterpart of a pure anisotropic Earth (i.e., a model where only the anisotropic component varies spatially) is $\mathcal{H}(\mathcal{A}(\mathbf{S})) = \mathcal{H}(\mathbf{S_0} + \mathbf{S_A})$ where $\mathcal{A}(\mathcal{H}(\mathcal{A}(\mathbf{S})))$ is the *effective intrinsic anisotropy*. The *effective intrinsic radial anisotropy* corresponding to $\mathcal{A}(\mathcal{H}(\mathcal{A}(\mathbf{S})))$ will then be designated as ξ^*_{CPO}. Note that due to the non-linearity of $\mathcal{H}$, homogenization creates apparent isotropic heterogeneities in the elastic tensor $\mathcal{I}(\mathcal{H}(\mathcal{A}(\mathbf{S})))$ as a byproduct, albeit of low amplitude.

Finally, the tomographic counterpart of a pure isotropic Earth (i.e., a model where the isotropic component varies spatially, and the anisotropic component is zero) is $\mathcal{H}(\mathcal{I}(\mathbf{S})) = \mathcal{H}(\mathbf{S_0} + \delta\mathbf{S_I})$ where the non-negligible apparent anisotropic component due to SPO $\mathcal{A}(\mathcal{H}(\mathcal{I}(\mathbf{S})))$ is called *extrinsic anisotropy*. Here, *extrinsic radial anisotropy* will be denoted by ξ^*_{SPO} (Refer to Figure 1 for a comprehensive summary).

3. Analytical Expressions in the 1-D Case

3.1. Backus Homogenization

A VTI medium is an elastic medium with hexagonal symmetry and vertical symmetry axis. It can be described by five elastic parameters A, C, F, L, and N, also known as the Love parameters (Love, 1906). Supposing that axis 3 is the symmetry axis, the local $\mathbf{S}$ for a VTI solid can be expressed in Mandel notation as:

$$\mathbf{S} = \begin{pmatrix} A & A-2N & F & 0 & 0 & 0 \\ A-2N & A & F & 0 & 0 & 0 \\ F & F & C & 0 & 0 & 0 \\ 0 & 0 & 0 & 2L & 0 & 0 \\ 0 & 0 & 0 & 0 & 2L & 0 \\ 0 & 0 & 0 & 0 & 0 & 2N \end{pmatrix}. \tag{5}$$

In a weakly anisotropic medium, $SV-$ and $SH-$ waves are sensitive to the elastic parameters L and N, respectively, according to the formula:

$$V_{SV} = \sqrt{\frac{L}{\rho}} \tag{6}$$

$$V_{SH} = \sqrt{\frac{N}{\rho}}, \tag{7}$$

where ρ is density. The level of $S-$wave radial anisotropy is controlled by the anisotropic parameter:

$$\xi = \left(\frac{V_{SH}}{V_{SV}}\right)^2 = \frac{N}{L}. \tag{8}$$

Backus (1962) explicitly showed analytical upscaling relations for seismic waves propagating in a 1-D stratified medium. For a 1-D layered medium where each layer is a VTI medium, the long-wavelength effective medium is also a VTI medium. The effective equivalent of the elastic constants, for instance, N and L concerning the shear wave velocities are given by an arithmetic mean and a harmonic mean, respectively:

$$N^* = \langle N \rangle, \tag{9}$$

$$L^* = \langle 1/L \rangle^{-1}, \tag{10}$$

where $\langle . \rangle$ refers to the spatial average over a wavelength of any periodic function (in this case, N and $1/L$), and * denotes a long-wavelength effective property. The effective density ρ^* is simply the arithmetic mean of the local density ρ:

$$\rho^* = \langle \rho \rangle. \tag{11}$$

The effective $S-$radial anisotropy ξ^* is essentially the ratio between the effective equivalents of N and L:

$$\xi^* = \frac{N^*}{L^*} = \langle N \rangle \langle 1/L \rangle. \tag{12}$$

In this way, for a 1-D fine-scale medium where each layer is isotropic ($N = L$), the long-wavelength effective medium is transversely isotropic, and the level of extrinsic radial anisotropy is given by $\langle N \rangle \langle 1/N \rangle$ (Alder et al., 2017).

3.2. An Analytical Expression to Quantify CPO and SPO in a 1-D Layered Media

Let us consider an intrinsically anisotropic (CPO component) and finely layered (SPO component) 1-D VTI medium. Assuming in the matrix (5), no $P-$wave anisotropy (i.e., $C = A$) and setting $F = A - 2L$, one can express the isotropic rigidity as (Maupin et al., 2007; Montagner, 2007):

$$\mu = \frac{1}{3}(2L + N). \tag{13}$$

Knowing Equations 8 and 13, one can re-write N and L in terms of μ and $\xi_{\text{CPO}} = N/L$ giving:

$$N = \xi_{CPO}\frac{3\mu}{2+\xi_{CPO}}, \tag{14}$$

$$L = \frac{3\mu}{2+\xi_{CPO}}. \tag{15}$$

To calculate the long-wavelength effective equivalent of such a medium, let us first write the parameters μ and ξ_{CPO} as:

$$\mu(z) = \langle\mu\rangle + \delta\mu(z), \tag{16}$$

$$\xi_{CPO}(z) = \langle\xi_{CPO}\rangle + \delta\xi_{CPO}(z), \tag{17}$$

where $\langle\mu\rangle$ and $\langle\xi_{CPO}\rangle$ are the spatially averaged counterparts. $\delta\mu$ and $\delta\xi_{CPO}$ are small-scale radial heterogeneities (i.e., layering) in the shear modulus and intrinsic radial anisotropy, respectively, where $\langle\delta\mu\rangle$ and $\langle\delta\xi_{CPO}\rangle = 0$.

The long-wavelength effective equivalents N^* and $1/L^*$ are:

$$N^* = \langle N\rangle = \left\langle \xi_{CPO}\frac{3\mu}{2+\xi_{CPO}}\right\rangle = \left\langle (\langle\xi_{CPO}\rangle + \delta\xi_{CPO})\frac{3(\langle\mu\rangle+\delta\mu)}{2+\langle\xi_{CPO}\rangle+\delta\xi_{CPO}}\right\rangle, \tag{18}$$

$$1/L^* = \langle 1/L\rangle = \left\langle \frac{2+\xi_{CPO}}{3\mu}\right\rangle = \left\langle \frac{2+\langle\xi_{CPO}\rangle+\delta\xi_{CPO}}{3(\langle\mu\rangle+\delta\mu)}\right\rangle. \tag{19}$$

We can simplify Equations 18 and 19 by assuming a weak contrast in the shear modulus $\delta\mu \ll \langle\mu\rangle$ and in the intrinsic radial anisotropy $\delta\xi_{CPO} \ll \langle\xi_{CPO}\rangle$. Using a second-order Taylor expansion, we get:

$$N^* \approx \frac{3\langle\mu\rangle}{2+\langle\xi_{CPO}\rangle}\left(\langle\xi_{CPO}\rangle - \frac{2\langle\delta\xi_{CPO}^2\rangle}{(2+\langle\xi_{CPO}\rangle)^2} + \frac{2\langle\delta\mu\cdot\delta\xi_{CPO}\rangle}{\langle\mu\rangle(2+\langle\xi_{CPO}\rangle)}\right), \tag{20}$$

$$1/L^* \approx \frac{2+\langle\xi_{CPO}\rangle}{3\langle\mu\rangle}\left(1 + \frac{\langle\delta\mu^2\rangle}{\langle\mu\rangle^2} - \frac{\langle\delta\mu\cdot\delta\xi_{CPO}\rangle}{\langle\mu\rangle(2+\langle\xi_{CPO}\rangle)}\right). \tag{21}$$

Note that we have used a parameter which is $\langle\xi_{CPO}\rangle = 1$ in the absence of intrinsic anisotropy in all layers. We could have used, instead, a parameter that cancels in the absence of intrinsic anisotropy, for example, the fractional change in shear wave velocities $\gamma = (V_{SH} - V_{SV})/V_S$ (e.g., Xie et al., 2013, 2017). This parameter is also used in the Thomsen notation (Bakulin, 2003; Thomsen, 1986) but the two parameters are simply related by $\gamma = 1 - \sqrt{\xi}$. We decide to keep ξ since this is the parameter that is most often used to describe large-scale mantle anisotropy.

Using Equation 12, we multiply Equations 20 and 21 and neglect terms higher than order 2 to obtain the full effective radial anisotropy ξ^* due to both fine-layering and intrinsic radial anisotropy:

$$\xi^* \approx \langle\xi_{CPO}\rangle - \frac{2}{(2+\langle\xi_{CPO}\rangle)^2}\langle\delta\xi_{CPO}^2\rangle + \frac{\langle\xi_{CPO}\rangle}{\langle\mu\rangle^2}\langle\delta\mu^2\rangle + \frac{2-\langle\xi_{CPO}\rangle}{\langle\mu\rangle(2+\langle\xi_{CPO}\rangle)}\langle\delta\mu\cdot\delta\xi_{CPO}\rangle. \tag{22}$$

Equation 22 explicitly shows the separate effects of the small scales in the isotropic component and in the intrinsically anisotropic component onto the effective radial anisotropy as "seen" by long-period seismic waves.

Assuming the medium to be devoid of intrinsic radial anisotropy (i.e., $\xi_{CPO} = 1$ and $\delta\xi_{CPO} = 0$), the full effective radial anisotropy ξ^* directly relates to the variance of small-scale heterogeneities $\langle\delta\mu^2\rangle$ in the shear modulus $\delta\mu$. It can be interpreted as the extrinsic radial anisotropy ξ^*_{SPO} due to the seismically unresolved small-scale isotropic heterogeneities. It varies as the square of the heterogeneities, in agreement with the result of Alder et al. (2017).

On the other hand, when the isotropic component is uniform (i.e., $\delta\mu = 0$), ξ^* also varies with the square of heterogeneities, but now in intrinsic radial anisotropy. This can be interpreted as the effective intrinsic radial anisotropy ξ^*_{CPO}, that is, the intrinsic radial anisotropy that gets smoothed out as a result of upscaling. Interestingly, its overall effect is to reduce the level of intrinsic radial anisotropy as indicated by the minus sign in front of the second term. In the absence of small-scale isotropic heterogeneities, we anticipate radial anisotropy to be always underestimated by tomography.

Finally, Equation 22 suggests the existence of a cross-term $\langle \delta\mu \cdot \delta\xi_{\mathrm{CPO}} \rangle$ due to the spatial correlation between intrinsic radial anisotropy and shear modulus. Supposing spatial variations in both components are significant such as at major seismic discontinuities, the correlation term should influence the anisotropy mapped in tomographic models.

Similarly, the effective Voigt-averaged shear modulus μ^* is given by:

$$\mu^* = \frac{2L^* + N^*}{3}. \tag{23}$$

Plugging Equations 20 and 21 into Equation 23, we get:

$$\mu^* = \langle \mu \rangle - \frac{2}{\langle \mu \rangle (2 + \langle \xi_{\mathrm{CPO}} \rangle)} \langle \delta\mu^2 \rangle - \frac{2\langle \mu \rangle}{(2 + \langle \xi_{\mathrm{CPO}} \rangle)^3} \langle \delta\xi_{\mathrm{CPO}}^2 \rangle + \frac{4}{(2 + \langle \xi_{\mathrm{CPO}} \rangle)^2} \langle \delta\mu \cdot \delta\xi_{\mathrm{CPO}} \rangle. \tag{24}$$

Ignoring intrinsic radial anisotropy (i.e., $\langle \xi_{\mathrm{CPO}} \rangle = 1$ and $\delta\xi_{\mathrm{CPO}} = 0$), the effective shear modulus μ^* is always smaller than its spatially averaged version $\langle \mu \rangle$. Such a result is logical in the 1-D case. Here, radial anisotropy induced by fine-layering is always positive (Equation 22) thereby having $N^* > L^*$. Since L "counts" two times and N once in its isotropic average, its long-wavelength effective equivalent μ^* is always slower than $\langle \mu \rangle$. Contrastingly, if one neglects isotropic heterogeneities and only consider variations in intrinsic radial anisotropy, homogenization also results in the underestimation of the shear modulus. One would predict that homogenization leads to the creation of apparent isotropic heterogeneities due to small-scale variations in CPO. Finally and as expected, the cross term recurs due to the spatial correlation between the shear modulus and intrinsic radial anisotropy.

Although the homogenized Equations 22 and 24 make clear that homogenization leads to correction terms that are only second-order, these effects may not be negligible. First, the equations that we obtained are also valid in situations where $\langle \xi_{\mathrm{CPO}} \rangle = 1$ but where $\langle \delta\xi_{\mathrm{CPO}}^2 \rangle$, $\langle \delta\mu^2 \rangle$, or $\langle \delta\xi_{\mathrm{CPO}} \delta\mu \rangle$ are different from zero, in which case, all observed anisotropy would be related to second-order effects. In the case of SPO, the variance in the shear modulus μ can be extreme in the presence of partial melt or water in the mantle (e.g., Auer et al., 2015; Hacker et al., 2003). An increase in seismic wave speed variations of about 20% underneath mantle wedges can result from the full hydration of peridotite and eclogite (Hacker et al., 2003). This may then significantly contribute to the effective radial anisotropy mapped in tomographic images. Contrastingly, significant second-order effects due to CPO-related radial anisotropy may only be possible if there are relatively fast spatial variations in intrinsic anisotropy. For instance, parts of the lithosphere, especially underneath oceanic basins, may harbor layering that is composed of frozen-in CPO transported from the ridge (Becker et al., 2008; Hansen et al., 2016; Hedjazian et al., 2017) and the isotropic mantle lithosphere. This layering may produce sharp spatial variations in intrinsic radial anisotropy. According to Equation 22, this would tone down the level of the observed radial anisotropy.

The homogenized expressions given by Equations 22 and 24 in terms of the isotropic shear modulus μ may not be particularly convenient for seismologists. In practice, spatial distributions in V_S, and not in μ, are observed. If one assumes that density is uniform, then $\delta\mu/\mu$ can be simply replaced by $2\delta V_S/V_S$. On the other hand, if one assumes that density increases with V_S, one could also establish long-wavelength effective expressions for V_S in the same manner as μ using simple empirical relations for density such as that of Tkalčić et al. (2006).

In the Earth's asthenosphere where large-scale anisotropy due to mantle deformation is prevalent, the expected shear modulus heterogeneities between mineralogical phases seem at most 10% (e.g., Stixrude & Jeanloz, 2015; Xu et al., 2008). To perform a numerical estimate, let us examine a stack of planar layers with alternating shear moduli values differing by 20% (Figure 2a, middle panel). The 1-D depth profiles depict periodic variations with layers of equal thicknesses of 20 km. Positive intrinsic radial anisotropy ($\xi = 1.2$) is prescribed in the even layers, whereas the odd layers are isotropic ($\xi = 1$) (Figure 2a, right panel). After upscaling over a wavelength much larger than 20 km, the resulting profiles for N^* and L^* are homogeneous, and simply given by their arithmetic and harmonic means, respectively (Figure 2a, left panel). Once the long-wavelength effective N^* and L^* are acquired, we can compute the full effective radial anisotropy ξ^* through Equation 12 (solid red line in Figure 2a, right panel), and the effective shear modulus μ^* through Equation 23 (solid red line in Figure 2a, middle panel). Figure 2b illustrates a different scenario where ξ only exists in the odd layers (Figure 2b, right panel). In essence when the shear modulus and intrinsic radial

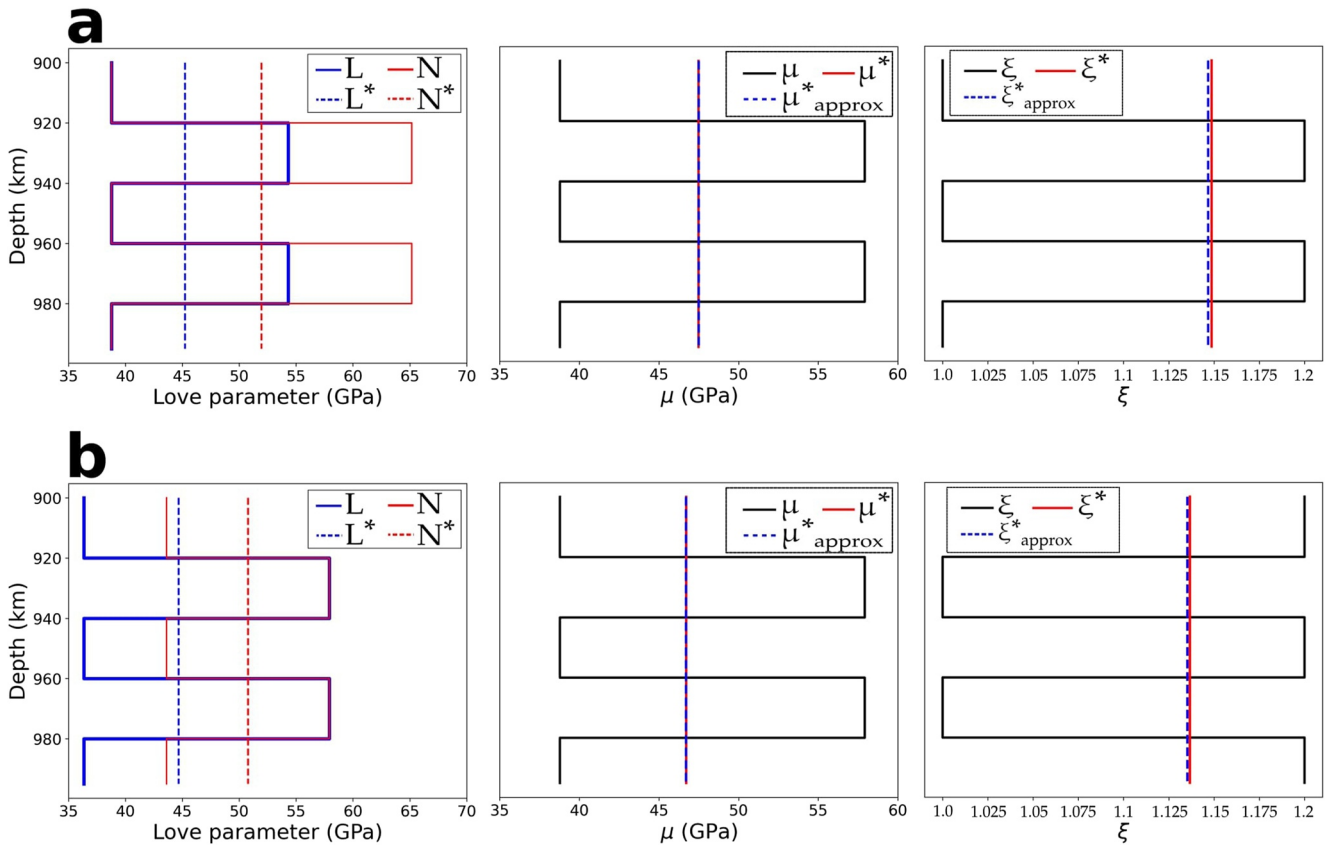

Figure 2. 1-D binary and periodic media with 20% isotropic heterogeneities in shear modulus prescribed across: (a) even layers, and (b) odd layers. Upon homogenization, the resulting profiles are homogeneous (variables denoted by [*]). The dashed blue lines at the middle (μ^*_{approx}) and right panels (ξ^*_{approx}) correspond to the predicted long-wavelength effective equivalents using the second-order approximations from Equations 24 and 22, respectively. The difference in the homogenized shear moduli and radial anisotropy between (a) and (b) is attributed to the cross term as implied by Equation 22. Since the medium is periodic, it is enough to only display a portion of the medium.

anisotropy are uncorrelated, the homogenized parameters μ^* and ξ^* should be the same regardless. However, a slight offset in μ^* and ξ^* of Figure 2b with respect to Figure 2a can be observed which is exclusively attributed to this cross term as hinted by Equations 22 and 24. Strictly speaking, the reduction in the amplitude of the effective properties arises from the switch in signs in the cross term from positive to negative $\langle \delta\mu \cdot \delta\xi \rangle$, implying that in the second scenario, the shear modulus and intrinsic radial anisotropy are anti-correlated.

To validate the second-order approximation, we also show ξ^* and μ^* using Equations 22 and 24, respectively (dashed blue lines in Figures 2a and 2b, middle and right panels). Clearly by applying Equation 22, the intrinsic component (first term) contributes the most to the effective radial anisotropy with $1 - \langle \xi_{\text{CPO}} \rangle = 0.1$. Its spatial variations' (second term) overall effect is to tone-down the amplitude of radial anisotropy by ~1%. This is followed by the SPO component (third term) which is responsible for the amplification of radial anisotropy by ~10%. Finally, the cross term provides the least contribution (less than ±1%) and therefore can reasonably be ignored in this case. The ± sign denotes that it may increase or decrease radial anisotropy depending on the coupling pattern between the shear modulus and intrinsic radial anisotropy.

3.3. Composite Law for S – Wave Radial Anisotropy

In this section, we show how the effective radial anisotropy can be expressed in terms of its intrinsic and extrinsic contributions. For that, we investigate two special cases: (a) a purely isotropic 1-D layered medium, (b) an anisotropic 1-D medium (i.e., no spatial variations in isotropic component), and find equivalent

expressions for extrinsic radial anisotropy ξ^*_{SPO} and effective intrinsic radial anisotropy ξ^*_{CPO}. By doing so, we elicit a simple composite law related to Equation 22 that can be extrapolated to 2-D and 3-D media.

In the case of an isotropic medium with spatially varying shear modulus, the radial anisotropy is entirely due to SPO. Equation 22 reforms into:

$$\xi^*_{SPO} \approx 1 + \frac{\langle \delta\mu^2 \rangle}{\langle \mu \rangle^2}. \tag{25}$$

On the other hand, an anisotropic medium without spatial variations in the shear modulus leads to an effective intrinsic radial anisotropy:

$$\xi^*_{CPO} \approx \langle \xi_{CPO} \rangle - \frac{2\langle \delta\xi^2_{CPO} \rangle}{(2 + \langle \xi_{CPO} \rangle)^2}. \tag{26}$$

By taking the product between Equations 25 and 26, neglecting terms higher than order 2, one has simply:

$$\xi^*_{CPO} \times \xi^*_{SPO} \approx \langle \xi_{CPO} \rangle - \frac{2\langle \delta\xi^2_{CPO} \rangle}{(2 + \langle \xi_{CPO} \rangle)^2} + \frac{\langle \xi_{CPO} \rangle \langle \delta\mu^2 \rangle}{\langle \mu \rangle^2}, \tag{27}$$

which is approximately equal to ξ^* in Equation 22 but without the cross term. Therefore, ignoring spatial correlations between intrinsic radial anisotropy and shear modulus, the full effective radial anisotropy can be quantified through the following composite law:

$$\xi^* \approx \xi^*_{CPO} \times \xi^*_{SPO}. \tag{28}$$

In practice, ξ^* can be estimated from a tomographic inversion (Debayle & Kennett, 2000; Fichtner et al., 2010; Gung et al., 2003; Nettles & Dziewoński, 2008; Plomerová et al., 2002). Seismologists often compare ξ^* with the intrinsic radial anisotropy ξ_{CPO} computed from a geodynamically based CPO model (Becker et al., 2003, 2006; Ferreira et al., 2019; Sturgeon et al., 2019). The comparison should be done instead with an effective model ξ^*_{CPO}, which is difficult to estimate without access to any elastic homogenization tools. Furthermore, Equation 22 suggests that there is a non-negligible extrinsic component of radial anisotropy due to the unresolved small-scale isotropic heterogeneities. While it is difficult to rigorously establish analytical solutions in the case of a 2-D/3-D complex media, following the logic above, we hypothesize that the mismatch often observed between homogenized CPO models and tomographic models is the extrinsic radial anisotropy ξ^*_{SPO}.

4. Methods for 2-D Media

4.1. Homogenization in 2-D and in 3-D Media

The classic homogenization method of Backus is only applicable in 1-D to media exhibiting spatial periodicity. The true Earth, however, is a complex 3-D and multi-scale medium. To alleviate this problem and quantify effective elastic properties in a mantle-like medium, we rely on the non-periodic elastic homogenization technique developed by Capdeville and Marigo (2007), Capdeville et al. (2010), Guillot et al. (2010), and Capdeville et al. (2015). Originally, this method has been developed as a pre-processing step enabling one to solve the elastostatic wave equation using a simple mesh, speeding up the computations for wave propagation in complex media. It has also been used to improve the convergence and computational cost of full-waveform inversion (Capdeville & Métivier, 2018; Hedjazian et al., 2021). Most homogenization methods rely on a "cell" problem: a set of static elasticity problems whose solutions are the base of the effective medium (Sanchez-Palencia, 1980). In the 1-D case, this "cell" problem has an analytical solution that leads to explicit formulas for the effective medium such as the one found in Backus (1962). In higher dimensions, this analytical solution does not exist and we need to rely on a numerical solver to obtain the solutions of the cell problem. Finite element methods are classically used for this purpose. Nevertheless, solvers based on the periodic Lippman-Schwinger equation and fast Fourier transforms (Moulinec & Suquet, 1998) can also be very efficient leading to a mesh-less tool (Capdeville et al., 2015).

In the non-periodic case, homogenization is not performed with respect to the periodicity of the medium, but with respect to the minimum wavelength present in the wavefield. The assumption that this minimum wavelength λ_{min} exists is required for non-periodic medium with no scale separation such as the true Earth.

Scales smaller than $\lambda_{\min}$ are seen by the wavefield only through their effective properties. To separate the small and the large scales, we need to define a threshold wavelength λ_h, called the homogenization wavelength. λ_h is a user-defined parameter, and all scales smaller than λ_h are homogenized. Numerical examples suggest that, for all natural media, homogenization with a value $\lambda_h = 0.5\lambda_{\min}$ is sufficient to accurately reproduce the complete wavefield (Capdeville et al., 2010). Hence, this value is chosen in the rest of the present study. Computing the effective properties of an elastic medium with homogenization wavelength λ_h requires to solve an elastostatic problem numerically. To do this, we use the 3-D Fast-Fourier Homogenization algorithm developed by Capdeville et al. (2015).

In practice, two factors prevent the recovery of the true Earth by tomographic methods: (a) limited frequency band of the recorded seismic signals, and (b) limited data coverage of ray paths. In the context of full-waveform inversions with perfect coverage (i.e., where sources and receivers are densely distributed at the surface of the volume to image), Capdeville and Métivier (2018) numerically verified that a seismic tomography model and the homogenized model are in agreement at spatial wavelengths longer than λ_h. Hence, homogenization can be viewed as a first-order tomographic operator assuming perfect data coverage. We will consider the homogenized model as the best image one could get from seismic tomography. This can be translated to:

$$\mathbf{S}^* = \mathcal{H}(\mathbf{S}) \tag{29}$$

where $\mathcal{H}$ is the tomographic operator, $\mathbf{S}$ is the true elastic structure, and the homogenized model $\mathbf{S}^*$ is the full effective medium (i.e., the best recovered image as seen by a wavefield of a given minimum wavelength $\lambda_{\min}$ and assuming perfect data coverage). In this paper, we apply this "tomographic operator" to a 2-D composite medium by upscaling the marble cake model in the presence of deformation-induced anisotropy. Note that the effect of limited data coverage could be simply accounted for by applying the tomography resolution matrix to $\mathbf{S}^*$ (Simmons et al., 2019). For simplicity, we ignore this effect in this work.

4.2. Isotropic Heterogeneities in a 2-D Mechanically Mixed Mantle

To define our 2-D incompressible flow model imitating mantle convection, we use a stream function similar to that of Alder et al. (2017):

$$\Psi(x,z,t) = \sin(a\pi z)\Big[\sin(b\pi x) + \alpha(t)\sin((b+1)\pi x) + \beta(t)\sin((b+2)\pi x)\Big] \tag{30}$$

where $\alpha(t)$ and $\beta(t)$ are sinusoidal functions of time that introduces chaotic mixing. The variables a and b relate to the number of distinguishable convection cells and are chosen arbitrarily. The form of the function Ψ ensures free-slip boundary conditions. Finally, the resulting velocity field is scaled using a reference value of 1 cm·yr^{-1}.

We replicate the marble cake patterns by deforming a circular anomaly at the center of the box using our prescribed flow field. To do this, control points that define the contour of the anomaly are advected using fourth-order Runge Kutta methods with variable time-stepping (Press et al., 1992). To achieve a final configuration for the anomaly, we define an advection mixing time T_{SPO}. Figure 3 illustrates the evolution of the pattern when subjected to the flow field defined in Equation 30. Setting $a = 1$, $b = 2$, and $T_{\text{SPO}} = 75$ My, we have a mechanically mixed medium with two characteristic convection cells.

Using the last panel of Figure 3, the binary system is defined by assigning a reference S-wave velocity value $V_{S_2} = 4.52$ km· s^{-1} to the yellow region, and $V_{S_1} = 3.7$ km· s^{-1} to the purple region so that the level of isotropic heterogeneities is given by $100\% \times (V_{S_1} - V_{S_2})/(V_{S_1} + V_{S_2})\Big) = 10\%$. P –wave velocities are computed by imposing a constant ratio $V_P/V_S = 1.7$ (Obrebski et al., 2010). Following the work of Tkalčić et al. (2006), we compute the density ρ using the empirical relation $\rho = 2.35 + 0.036(V_P - 3)^2$. These values are used to define the local isotropic tensor $\mathbf{S_I}$ in Equation 1.

4.3. Modeling of Crystallographic Preferred Orientation

Using the velocity gradient tensor derived from the stream function Ψ described previously, we then model CPO evolution of olivine aggregates using D-Rex, a program that calculates strain-induced CPO by plastic

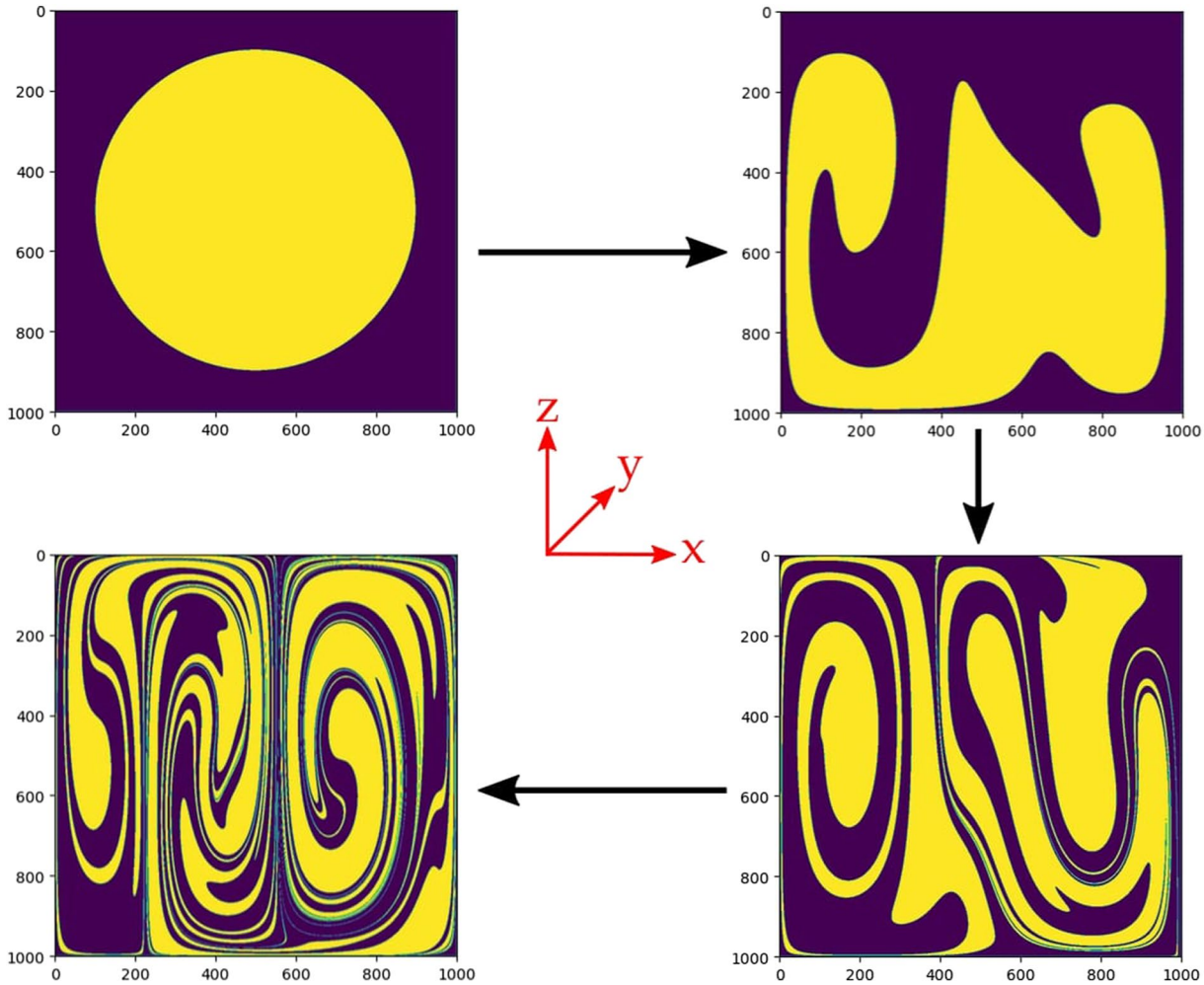

Figure 3. Initially a circle, the anomaly is deformed progressively until the medium reaches a stage resembling marble cake-like patterns.

deformation, and dynamic recrystallization (Kaminski et al., 2004). The activities of olivine slip systems are chosen to correspond to dry mantle conditions, while other parameters are taken as in the reference D-Rex model. To control the level of intrinsic anisotropy, we assume that CPO only developed in the last T_{CPO} of the simulation.

In our numerical experiments, we compute CPO everywhere irrespective of the actual mineralogical phase. We scale the elastic tensor derived from D-Rex so that its isotropic component is identical to the binary system derived in Section 4.2. The true elastic structure can be constructed from Equation 1 where $\mathbf{S_I}$ now relates to the small-scale isotropic heterogeneities in the mechanically mixed mantle, and $\mathbf{S_A}$ is the intrinsically anisotropic component computed with D-Rex.

4.4. Quantifying the Level of Anisotropy

In this section, we define two ways to quantify the level of seismic anisotropy for any given elastic tensor **S**. The first one is radial anisotropy. We project the elastic tensor in terms of an azimuthally averaged VTI medium to obtain a tensor described as in Equation 5. Here, the parameters L and N can be computed from **S** as follows (Montagner & Nataf, 1986):

$$L = \frac{1}{2}(S_{44} + S_{55}) \tag{31}$$

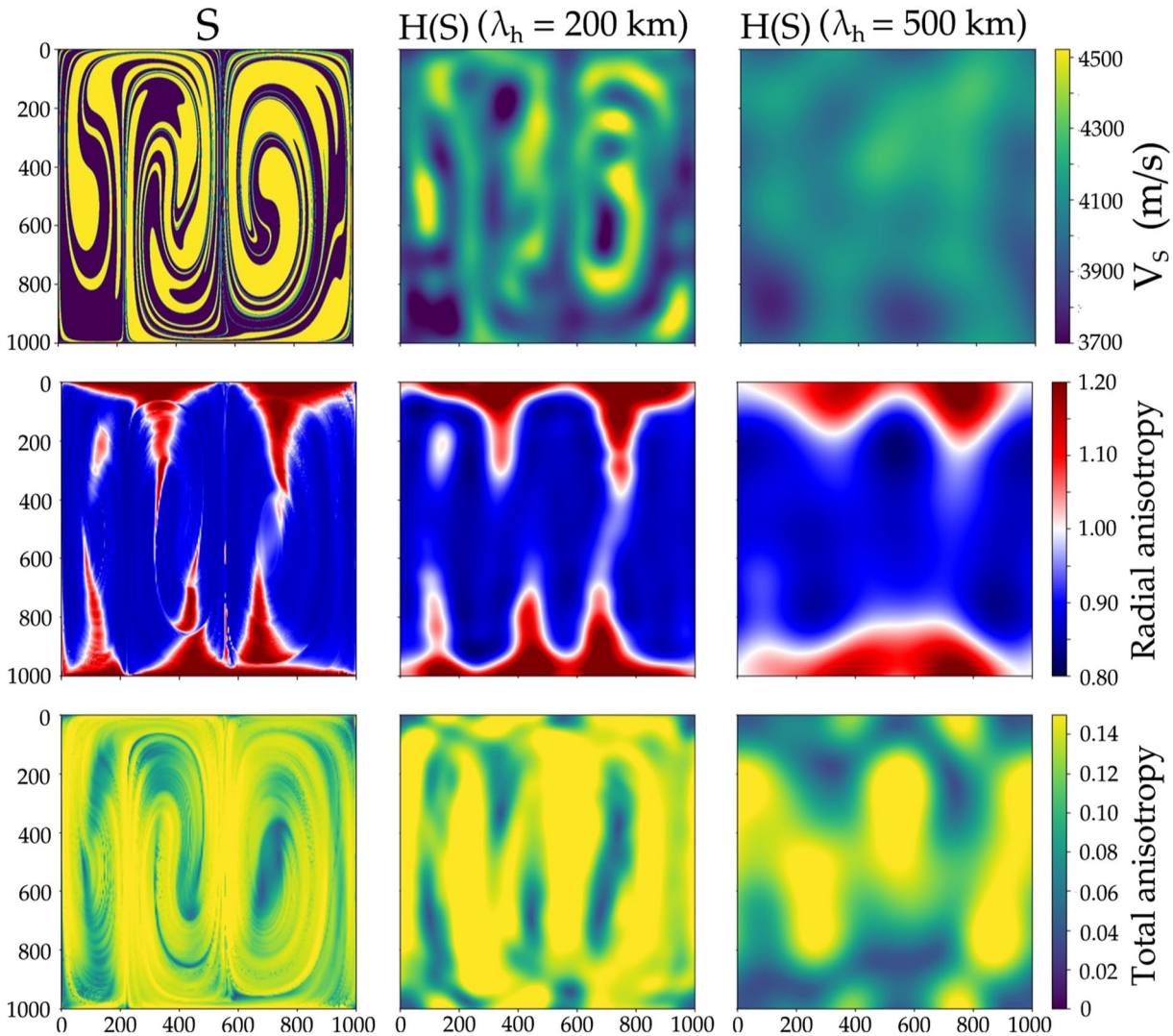

Figure 4. Seismic properties of the true elastic structure **S** before and after homogenization. The model dimensions are 1,000 km × 1,000 km. Here, each pixel contains an **S** which consists of small-scale isotropic heterogeneities and an intrinsically anisotropic perturbation computed with D-Rex (Kaminski et al., 2004). The present-day marble cake patterns correspond to a mixing time for advection $T_{SPO} \sim 75$ My, whereas the time scale for CPO evolution is $T_{CPO} \sim 40$ My. We homogenized **S** using the Fast-Fourier homogenization algorithm of Capdeville et al. (2015). (From left to right) First row: V_s models derived from **S**, $\mathcal{H}(\mathbf{S})$ at $\lambda_h = 200$ km, and $\mathcal{H}(\mathbf{S})$ at $\lambda_h = 500$ km. Second row: ξ_{CPO}, ξ^* at $\lambda_h = 200$ km, and ξ^* at $\lambda_h = 500$ km. Last row: Total anisotropy in terms of the norm fraction of **S**, $\mathcal{H}(\mathbf{S})$ at $\lambda_h = 200$ km, and $\mathcal{H}(\mathbf{S})$ at $\lambda_h = 500$ km. Elastic homogenization can be viewed as the best possible model reconstructed by seismic tomography assuming perfect ray-path coverage.

$$N = \frac{1}{8}(S_{11} + S_{22}) - \frac{1}{4}S_{12} + \frac{1}{2}S_{66}. \tag{32}$$

The level of radial anisotropy is then given by Equation 8.

Another convenient way to quantify anisotropy is to compute the percentage of total anisotropy by taking the L2-norm fraction of the anisotropic part of the elastic tensor with respect to the isotropic part. This quantity is called the anisotropy index and is given by:

$$\text{anisotropy index} = \frac{\|\mathbf{S} - \mathbf{S_I}\|}{\|\mathbf{S_I}\|}. \tag{33}$$

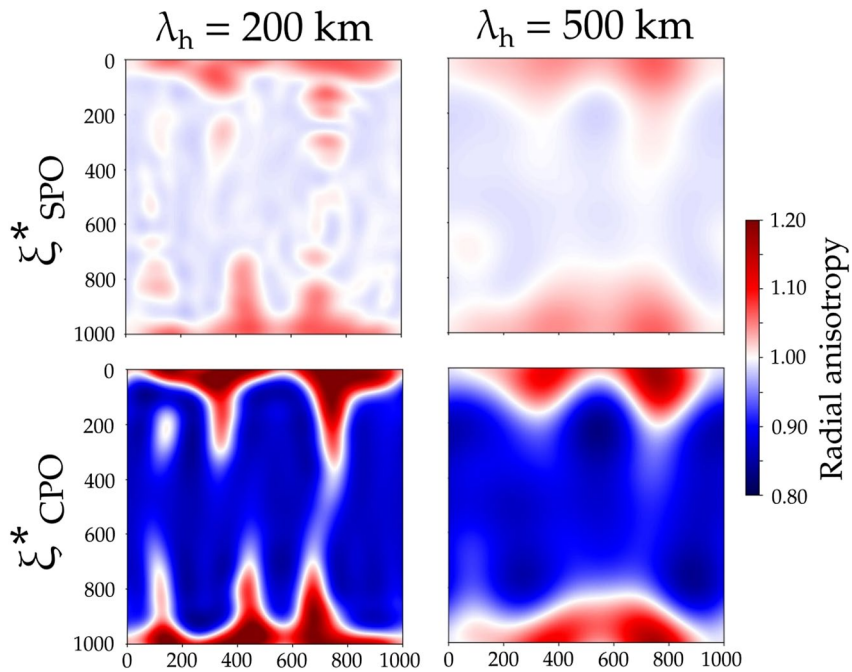

Figure 5. Extrinsic radial anisotropy ξ^*_{SPO} (i.e., radial anisotropy of model $\mathcal{H}(\mathcal{I}(\mathbf{S}))$) (top panels) at two different wavelengths of homogenization λ_h. It is computed following the projection of the homogenized elastic tensor into an azimuthally averaged VTI tensor as "seen" by surface waves (Montagner & Nataf, 1986). Here, $\xi^*_{SPO} > 1$ is now interpreted as horizontal layering whereas <1 as vertical layering. The bottom panels show the effective intrinsic radial anisotropy ξ^*_{CPO} (i.e., radial anisotropy of model $\mathcal{H}(\mathcal{A}(\mathbf{S}))$).

5. Elastic Homogenization of a 2-D Mechanically Mixed Mantle in the Presence of CPO

Figure 4 displays some seismic properties of the true elastic structure **S** before and after homogenization in a 1,000 km × 1,000 km box. The left panels are the true structures, whereas the middle and right panels are the structures equating to the full effective medium $\mathcal{H}(\mathbf{S})$ at homogenization wavelengths λ_h of 200 and 500 km, respectively. The first row depicts the S −wave velocities, the second, the radial anisotropy, and the third, the anisotropy index. Each pixel initially contains an isotropic part derived from the marble cake model with a mixing time for advection $T_{SPO} \sim 75$ My, and an anisotropic part computed from a CPO model with a time scale for CPO evolution of $T_{CPO} \sim 40$ My corresponding to a moderately developed crystal fabric.

Several glaring features can be observed such as the presence of positive radial anisotropy ($\xi > 1$) at the top and bottom boundaries where flow is sub-horizontal, and likewise negative ($\xi < 1$) at regions where the flow is sub-vertical. As expected, homogenization results in the smoothing of the structures with the level of smoothing modulated by λ_h. However, homogenization is not just a simple spatial average but a product of highly non-linear upscaling relations. With increasing homogenization wavelengths, the full effective medium becomes devoid of anisotropy in some areas.

After decomposing **S** into an isotropic tensor $\mathcal{I}(\mathbf{S})$ and an anisotropic tensor $\mathcal{A}(\mathbf{S})$ through Equations 2 and 4, one can also homogenize and analyze each component separately, that is, $\mathcal{H}(\mathcal{I}(\mathbf{S}))$ and $\mathcal{H}(\mathcal{A}(\mathbf{S}))$. Figure 5 shows the level of effective radial anisotropy of these two separate components after homogenization. The top panels recreate the results of Alder et al. (2017). Indeed, homogenizing the fine-layered isotropic medium produces extrinsic radial anisotropy ξ^*_{SPO} (i.e., radial anisotropy of model $\mathcal{H}(\mathcal{I}(\mathbf{S}))$). Notice that the patterns of effective intrinsic radial anisotropy and extrinsic radial anisotropy maps are roughly similar. For example, they both induce a positive radial anisotropy $\xi > 1$ in the horizontal layers: the stretched heterogeneities that induce SPO become elongated along the direction of the maximum principal strain rate that also controls the CPO.

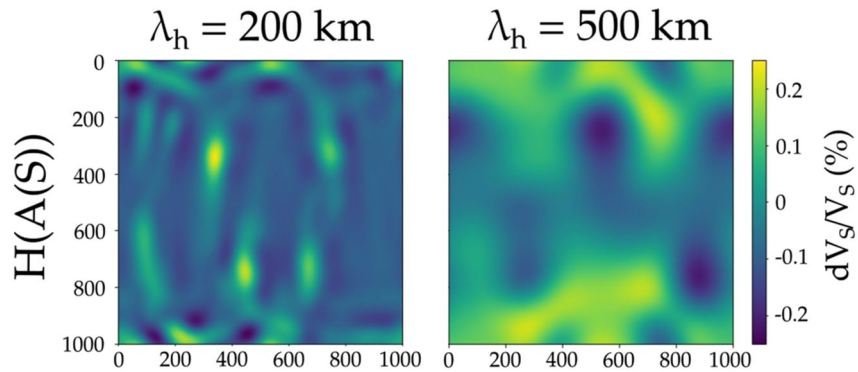

Figure 6. Apparent isotropic velocity perturbations with respect to a mean velocity V_S at two different wavelengths of homogenization λ_h. $\mathcal{H}(\mathcal{A}(\mathbf{S}))$ pertains to the homogenized model of an anisotropic medium. Even when placed in a very favorable scenario for intrinsic anisotropy, homogenizing an anisotropic medium produces a meager 0.25% artificial heterogeneities at $\lambda_h = 200$ km and 0.2% at $\lambda_h = 500$ km.

Figure 6 depicts the apparent isotropic heterogeneities created upon homogenization of $\mathcal{A}(\mathbf{S})$. It produces maximum velocity perturbations of about 0.25 % at $\lambda_h = 200$ km and 0.2 % at $\lambda_h = 500$ km. It appears to be a small effect, especially considering the large and sharp variations of intrinsic anisotropy in our CPO model.

To better illustrate the behavior of different contributions to radial anisotropy, we plot in Figure 7 the amplitude of radial anisotropy (in terms of its standard deviation over the entire 2-D model domain) against the wavelength of homogenization λ_h. In the following cases, the intrinsic anisotropy component of **S** is

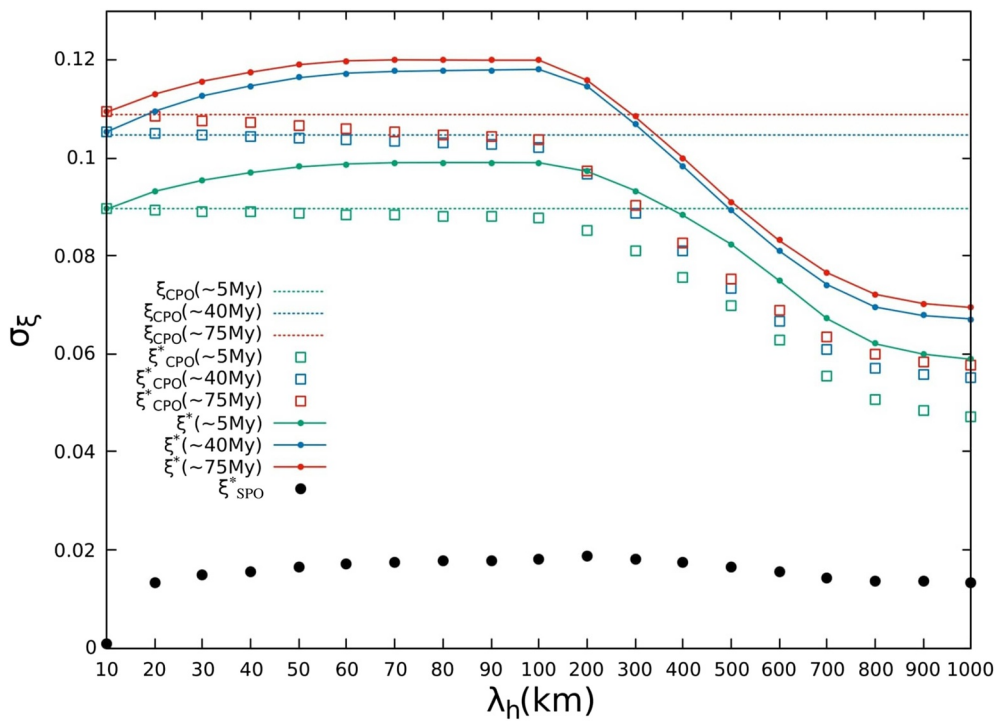

Figure 7. Effective radial anisotropy in terms of its standard deviation σ_{ξ} over the entire 2-D image, plotted as a function of homogenization length. The time scales indicated in million years pertain to the evolution history of CPO (a larger time scale leads to stronger CPO). Dashed lines represent the standard deviation of ξ_{CPO} in model **S** and serve as reference values. In this experiment, ξ^*_{SPO} of model $\mathcal{H}(\mathcal{I}(\mathbf{S}))$ (black circles) deemed to be five times smaller than ξ^*_{CPO} of model $\mathcal{H}(\mathcal{A}(\mathbf{S}))$ (hollow squares). Since SPO is mostly in-phase with CPO, the two anisotropic components add constructively giving the full effective radial anisotropy ξ^* (solid line-dots).

computed for a CPO developing over increasing duration T_{CPO} of 5, 40, or 75 Myr. Several points can be noted in Figure 7:

1. The resulting intrinsic radial anisotropy ξ_{CPO} in terms of its standard deviation over the entire region (dashed lines) increases with T_{CPO}, although some saturation is observed (i.e., the orientation of crystals depends mostly on their recent deformation, and lose the memory of the deformation they underwent too long ago).
2. The level of intrinsic radial anisotropy is diminished upon homogenization. ξ^*_{CPO} (hollow squares) is always lower than the reference value ξ_{CPO} (dashed lines), and diminishes with λ_h. This effect can be easily understood. For small λ_h, the wavelength of homogenization is small compared to the scale of deformation patterns (of order 100 km). At each point of the 2-D map, the direction of CPO is therefore locally constant over λ_h, which yields $\xi^*_{CPO} \approx \xi_{CPO}$. At larger scales, when λ_h increases compared to the scale of convection, this direction becomes likely random and CPO heterogeneities averaged over λ_h have different orientations: there is less of a preferential direction and the averaged level of CPO anisotropy is diminished.
3. On the contrary, the full effective radial anisotropy ξ^* at short wavelengths of homogenization λ_h is larger than ξ_{CPO}. This is in agreement with the analytical expression given by Equation 22. This additional anisotropy is of course due to the existence of SPO (black circles) which reinforces the total level of effective radial anisotropy.
4. Both ξ^*_{CPO} and ξ^* converge toward ξ_{CPO} at infinitely short homogenization wavelengths. Only in this unrealistic case (i.e., the perfect recording of the seismic wavefield up to infinitely short periods), would seismic tomography be able to map the true intrinsic radial anisotropy.
5. Extrinsic radial anisotropy ξ^*_{SPO} here has an amplitude that is five times smaller than ξ^*_{CPO}. Such a result, of course, is specific to this numerical experiment, and that CPO is indeed stronger than SPO might not be always true. For instance, a longer mixing time would have resulted in a thinner and more complex layering that would have increased the SPO. We are unfortunately limited by the number of tracers necessary to describe the phase stirring which is exponentially increasing with time.

5.1. Verifying the Composite Law $\xi^* = \xi^*_{CPO} \times \xi^*_{SPO}$ in 2-D

In this section, we aim to numerically verify Equation 28 in 2-D by plotting $\xi^*_{SPO} \times \xi^*_{CPO}$ against ξ^* for each pixel in our 2-D maps of radial anisotropy. Here again, the three quantities ξ^*_{SPO}, ξ^*_{CPO}, and ξ^* are respectively computed from $\mathcal{H}(\mathcal{I}(\mathbf{S}))$, $\mathcal{H}(\mathcal{A}(\mathbf{S}))$, and $\mathcal{H}(\mathbf{S})$. We emphasize that since CPO is computed everywhere, there are no CPO discontinuities between the yellow and the purple stripes of our 2-D marble cake model; the radial anisotropy is almost uniform across thin laminations. Since the cross-term in Equation 22 depends on small-scales in ξ_{CPO}, we expect that there should be minimal spatial correlation between CPO and isotropic heterogeneities, and thus the effect of the cross-term is effectively mitigated. Figure 8b shows this for two different homogenization wavelengths λ_h. We can see that the relation holds exceptionally well even for large λ_h.

In practice, however, tomographic models of ξ^* are interpreted in terms of intrinsic anisotropy, and directly compared with ξ_{CPO} computed from CPO models (Becker et al., 2003, 2006; Ferreira et al., 2019). We mimic this scenario by comparing $\xi^*_{SPO} \times \xi_{CPO}$ instead with ξ^* (Figure 8a). As it turns out, the relation only holds for small values of λ_h. At larger values of λ_h, the trend appears to be more dispersed as a consequence of the averaging process, losing its viability to some extent. In the absence of a homogenized CPO model, we project that this composite law would remain true in general under the condition that the minimum wavelength used in tomography is sufficiently small.

To test the effect of the rigidity-anisotropy cross-term, we consider another mantle model where CPO is only present in one of the two phases of the 2-D marble cake illustrated in Figure 3. We impose that the purple component remains isotropic and we increase the percentage of isotropic heterogeneities in V_S to 15%. These two modifications would increase the correlation between the shear modulus and intrinsic radial anisotropy following Equation 22. Figure 8c displays the numerical solution at $\lambda_h = 50$ and 200 km when CPO is computed in the yellow phases alone. In this scenario, CPO now varies sharply and in the same places as isotropic discontinuities (i.e., $\delta\xi_{CPO}$ terms in Equation 22 are much larger), and as expected the cross-term is much more apparent. Nonetheless, this only produces small departures from the composite law (red line), implying that the predictions carried out by the composite law are robust.

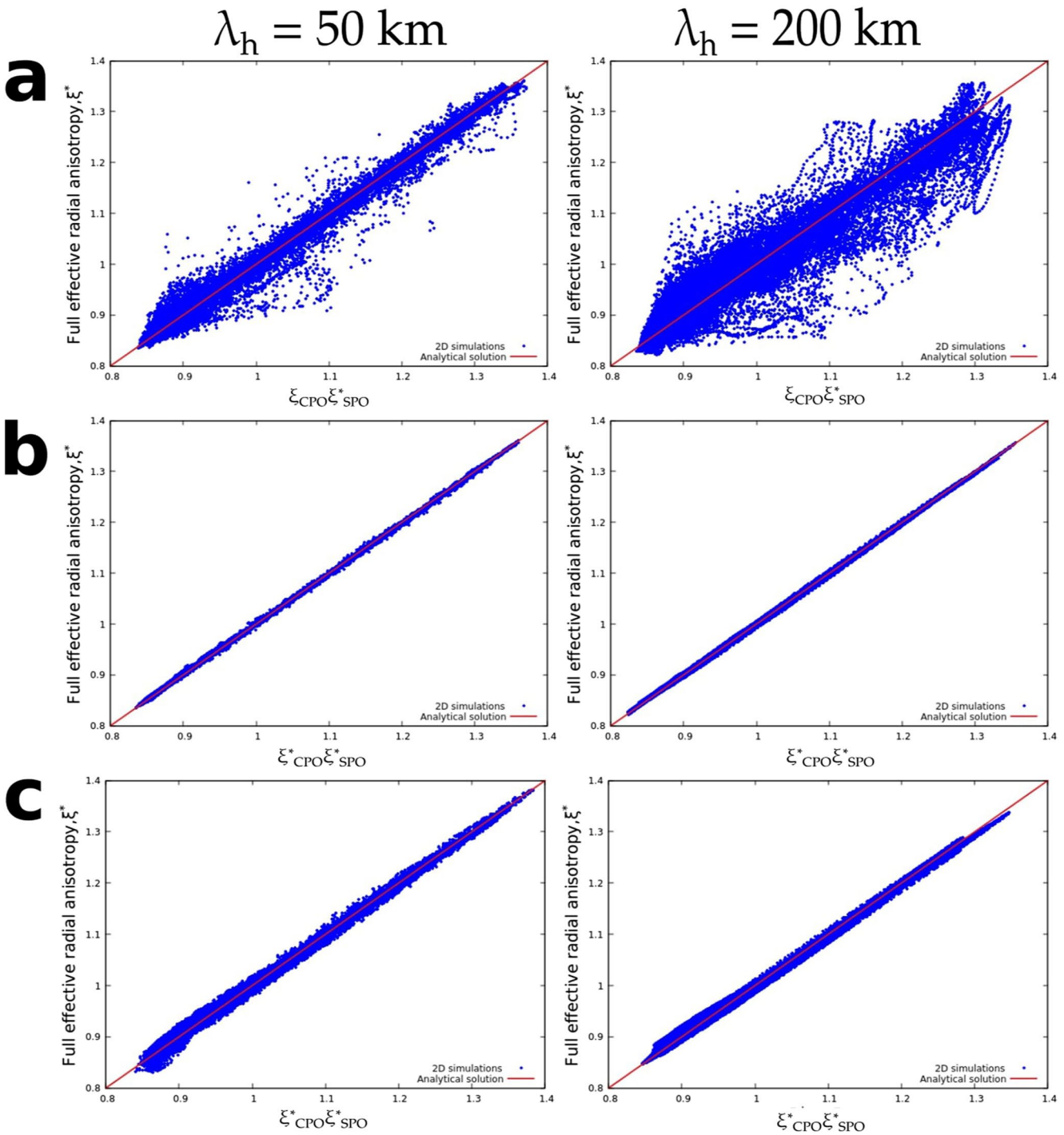

Figure 8. Panel (a): plot of the full effective radial anisotropy ξ^* as a function of $\xi_{\mathrm{CPO}} \times \xi^*_{\mathrm{SPO}}$. CPO is computed everywhere in this case. The media $\mathbf{S}$ and $\mathcal{I}(\mathbf{S})$ are homogenized at wavelengths of 50 km (left panel) and 200 km(right panel) to obtain ξ^* and ξ^*_{SPO}, respectively. Panel (b): the full effective radial anisotropy is now plotted against $\xi^*_{\mathrm{CPO}} \times \xi^*_{\mathrm{SPO}}$. The dispersion of the data is immensely reduced when the CPO is homogenized according to Equation 28. Panel (c): the purple phase is now assumed isotropic and the isotropic heterogeneities are increased to 15%. The cross-term, neglected in Equation 28, increases moderately the dispersion compared to panel (b).

5.2. Discussion

We investigated the effects of elastic homogenization to a specific class of fine-scale, marble cake-like models of the mantle in the presence of deformation-induced anisotropy. The homogenization procedure can be viewed as a tomographic operator applied to a reference elastic model (Capdeville et al., 2013).

We showed that the extrinsic radial anisotropy produced by fine-layering could reach up to 2% (see Figure 7) assuming 10% of isotropic heterogeneities. This radial anisotropy is much lower than the one induced by CPO where the effective intrinsic radial anisotropy could peak at nearly 11%. This result is however modulated by some parameters that regulate the level of effective radial anisotropy. For example, the layered filaments contrived from our marble cake models are of the order $10-100$ km whereas of those proposed by Allègre and Turcotte (1986) are much thinner and can stretch even further down to the centimeter scale. Because heterogeneities in a mechanically-mixed mantle follow a $1/k$ power spectrum (where k is wavenumber) (Alder et al., 2017; Mancinelli et al., 2016; Ricard et al., 2014), meaning that heterogeneities exist at all scales, thinner filaments may induce larger extrinsic radial anisotropy by increasing the volume of the mantle where homogenized heterogeneities produce SPO. In addition, effective anisotropy is also affected by the level of intrinsic anisotropy. Since CPO results from finite strain accumulation over time, the amplitude of intrinsic anisotropy increases with the time scale for CPO evolution T_{CPO}. Such presumptions may only be valid in regions where rock deformation varies over extended periods of time, although recrystallization and damage would limit the CPO that can be eventually accumulated (Ricard & Bercovici, 2009). Furthermore, we considered olivine of type-A crystal fabric as the solitary anisotropic mineral in our mantle models. Because of this, the intrinsic anisotropy produced from finite deformation should be seen as an upper bound. Inclusion of other anisotropic minerals such as pyroxene which make up a fraction in mantle peridotite (Maupin & Park, 2015) would change the net anisotropy. For instance, we anticipate that including a substantial amount of enstatite would dilute the amount of anisotropy (e.g., Kaminski et al., 2004). Therefore, whether CPO accounts for most of the bulk anisotropy observed in tomographic images remains inconclusive and needs further verification.

In light of the simulations conducted, we expect large-scale anisotropy to be only overestimated when CPO coexists with significant SPO as exemplified in our simulations. In the absence of SPO, homogenization can only decrease the strength of anisotropy. By accounting for both contributions, we showed that $\xi > 1$ is attributed to a combination of lateral flow and horizontal layering, and $\xi < 1$ is a combination of flow ascent and vertical layering. Indeed, the direction of shear not only dictates the preferred orientation of the anisotropic minerals, but also of the orientation of the folded strips that gives rise to fine-layering and SPO.

The repercussion of homogenizing intrinsic anisotropy alone amounts to the convection-scale averaging of the CPO as evidenced by our simulations. When long-period observations sample an intrinsically anisotropic medium, the wavefield spatially averages these orientations. As a result, preferential orientations that are products of imbricated convection tend to appear more heterogeneous, thereby ostensibly losing intrinsic anisotropy upon homogenization. In contrast, spatially coherent preferential orientations produced by simpler convection patterns are less susceptible to the dilution of intrinsic anisotropy.

The applicability of Equation 28 in 2-D complex media may be of interest to geodynamicists and tomographers alike. Not only does it permit one to directly quantify the discrepancy between the full effective radial anisotropy inferred from a tomographic model and the effective intrinsic radial anisotropy computed from a homogenized CPO model, it further solidifies the supposition that the mismatch is indeed a result of extrinsic radial anisotropy due to the seismically unresolved small-scale isotropic heterogeneities. We have conducted several numerical experiments to show that the composite law still holds even when the rigidity-intrinsic anisotropy cross term is amplified. However, the fact that the effect of the cross term is small may not be true for all cases, and thus caution must still be undertaken when applying the composite law.

The conclusions reached in this section are based on a number of simplifying assumptions: (a) The current forms of the homogenized analytical expressions given by Equations 22 and 24 neglect P –wave anisotropy. Our argument was based on how P –wave-related structures are poorly constrained by long-period tomography. However, Fichtner et al. (2013) showed that the effective S –wave radial anisotropy of an isotropic-equivalent medium (i.e., fine-layering) also depends on P –wave anisotropy. They concluded that some small-scale isotropic equivalents that give rise to extrinsic anisotropy may be eliminated in the picture if

P –wave anisotropy is known with considerable precision. Thus, further developments in our study should address this point. (b) We held the isotropic velocity contrast at a fixed value and assumed it to be representative of the entire mantle. In reality however, V_S variations generally decrease with depth (Stixrude & Jeanloz, 2015; Xu et al., 2008). This is not to mention the local presence of melt and water that contributes to the variations in wave velocities, and hence the strength of heterogeneities which completely alters the level of apparent anisotropy. (c) We disregarded the dependency of the elastic constants built from our mantle models on pressure P and temperature T. Future avenues one could take would be to incorporate $P-T$ dependence using empirical relations constrained from laboratory experiments. For instance, one may compute $P-T$ dependence using first-order corrections around a reference elastic tensor at ambient $P-T$ conditions (Estey & Douglas, 1986). The availability of self-consistent thermodynamic models based on free-energy minimization schemes (Connolly, 2005, 2009) can also be employed in lieu of the simpler relations for more accurate predictions of seismic wave velocities in any given bulk composition (Stixrude & Lithgow-Bertelloni, 2011).

6. Separating SPO From CPO in Tomographic Models: Application to Radial Anisotropy Beneath Oceanic Plates

Following the verification of the composite law in a 2-D complex medium, in this section, we present its application to a real-Earth problem. Here, our goal is to assess the discrepancy between a tomographic model and a CPO model of upper-mantle radial anisotropy underneath a mid-ocean ridge. In our hypothesis, this difference should be explained by the extrinsic radial anisotropy due to the unresolved small scales in seismic velocities.

6.1. Radial Anisotropy Beneath Oceanic Plates

Within the context of seismic tomography, surface waves offer the capability to image upper-mantle structure providing an in-depth view of large-scale anisotropy (e.g., Rychert et al., 2018). Surface wave tomography images positive radial anisotropy underneath oceanic basins ($V_{SH} > V_{SV}$), characterized by a layer of strong signatures lying in between ~80 – 200 km depth, corresponding to the asthenosphere (e.g., Ekström & Dziewonski, 1998; Montagner, 1985; Nettles & Dziewoński, 2008; Panning & Romanowicz, 2006). The maximum positive vertical gradient of ξ^*, at ~80 km depth, independent of plate age, is a recurrent feature in these tomographic models. This has raised questions about the potential use of radial anisotropy as a marker of the lithosphere-asthenosphere boundary, which is expected on the contrary to deepen with plate age (Beghein et al., 2019; Burgos et al., 2014; Rychert & Shearer, 2011). The strong radial anisotropy in the asthenosphere is usually explained by geodynamic models including CPO evolution (Becker et al., 2006, 2008).

Across the oceanic lithosphere, plate-averaged radial anisotropy (i.e., all points in the radial anisotropy models with the same plate age are averaged) displays modest levels of about 1–3%. Several models have been proposed to explain these observations. Hansen et al. (2016) and Hedjazian et al. (2017) suggest that CPO-related radial anisotropy developed below the ridge is subsequently frozen in the lithosphere, leading to an age-independent signature. It has also been proposed quasi-laminated melt structures, preserved during lithospheric thickening, can also explain this frozen-in signature of anisotropy (e.g., Auer et al., 2015; Debayle et al., 2020). Hence SPO may also be a potential explanatory mechanism, and a substantial fraction of the observed lithospheric anisotropy may be due to small-scale isotropic heterogeneities (Kennett & Furumura, 2015; Wang et al., 2013).

6.2. The Tomographic Model

In conjunction with the pre-existing global V_{SV} model of the upper-mantle constrained from Rayleigh wave data DR2012 (Debayle & Ricard, 2012), we adopt the recent global V_{SH} model CAM2016SH of Ho et al. (2016) to acquire a plate-averaged 2-D profile of radial anisotropy associated with slow-spreading oceanic ridges.

The V_S models were reconstructed by independently inverting Love (for V_{SH} models) and Rayleigh (for V_{SV} models) waveforms up to the fifth overtone between the period range 50 – 250 s using an extension of

the automated waveform inversion approach of Debayle (1999). We refer the reader to Debayle and Ricard (2012) and Ho et al. (2016) for a more detailed description of the inversion procedure.

From the V_{SV} and V_{SH} models of the upper-mantle, we compute the tomographic counterpart of radial anisotropy using $\xi^* = (V_{SH}/V_{SV})^2$. Here, ξ^* is not directly inferred from simultaneous inversions of Love and Rayleigh data but is a rudimentary estimate from the two S –wave velocity models that may conceivably have different qualities. We view the following exercise as only a proof-of-concept and therefore the results should be interpreted with caution.

The depth distribution of ξ^* spanning from 35 – 400 km is shown in Figure 9 (top panel). Positive radial anisotropy values ($\xi^* > 1$) are confined in the upper ~200 km of the model domain which is in close agreement with previous studies (e.g., Ekström & Dziewonski, 1998; Montagner, 1985; Panning & Romanowicz, 2006). Although the origin of anisotropy imaged in the asthenosphere is well-understood purely in terms of CPO, anisotropy observed in the lithosphere may be a combination of CPO and SPO (Wang et al., 2013). Here, our task is to invoke the composite law to isolate SPO from CPO in this tomographic model with the help of a homogenized CPO model.

6.3. The CPO Model

In this section, we re-interpret the results of Hedjazian et al. (2017) where they examined radial anisotropy profiles predicted from CPO models produced by plate-driven flows underneath a mid-ocean ridge. From their work, we borrowed two CPO models that correspond to a fast-developing CPO and a slow-developing CPO. The rate is dictated by the dimensionless grain boundary mobility parameter M which controls the kinetics of grain growth (and hence, the degree of dynamic recrystallization) (Kaminski et al., 2004). In the first case, a value of $M = 125$ constrained from laboratory experiments (Nicolas et al., 1973; Zhang & Karato, 1995) corresponding to CPO produced from uniform deformation and initially random CPO was imposed (Kaminski et al., 2004). Subsequently, the second case considers a case where $M = 10$ (i.e., slower CPO evolution) which also reproduces experimental results but in the case of an initially developed CPO (Boneh et al., 2015). We homogenize the two CPO models, obtain their long-wavelength effective equivalent, and appraise the resulting profiles in comparison with the tomographic model.

6.3.1. The Intrinsic CPO Mineralogical Model

2-D surface-driven mantle flows were acquired using the code Fluidity (Davies et al., 2011). In both models, upper-mantle deformation is governed by a composite dislocation and diffusion creep rheology following the implementation of Garel et al. (2014). D-Rex was used to model CPO evolution. A complete description of the methodology can be found in Hedjazian et al. (2017).

Figure 9 displays the intrinsic radial anisotropy profiles ξ_{CPO} belonging to the fast-evolving CPO with reference D-Rex values $M = 125$ (model A) and the slow-evolving CPO with $M = 10$ (model B). Model A predicts a layer with strong levels of intrinsic radial anisotropy of about 10% ($\xi_{\mathrm{CPO}} \approx 1.1$) at a depth of ~ 80 km starting at approximately 20 My. At about the same depth, tomographic models yield approximately 5% radial anisotropy (e.g., Burgos et al., 2014; Nettles & Dziewoński, 2008; Panning & Romanowicz, 2006). Hence, it has been argued that model A overpredicts the observed level of large-scale anisotropy in the upper-mantle (Hedjazian et al., 2017). On the contrary, model B predicts modest levels of intrinsic radial anisotropy, about 5% ($\xi_{\mathrm{CPO}} \approx 1.05$) across the oceanic lithosphere which is more consistent with tomographic observations. In total agreement with Hedjazian et al. (2017), these models apparently favor a low grain boundary mobility.

6.3.2. The Homogenized CPO Model

Figure 9 now shows the effective intrinsic radial anisotropy profiles ξ^*_{CPO} of model A* and model B*. In both cases, the ensuing patterns of radial anisotropy are smoothed out as a result of homogenization and more so for the fast mobility model A which predicts a shallow CPO. For instance, the apparent two-layered distribution of intrinsic radial anisotropy with depth (down to ~250 km) in model A vanishes after homogenization. The depth profile of effective intrinsic radial anisotropy as a result contains one layer of radial anisotropy centered at ~100 km depth, making it now compatible with tomographic models of the asthenosphere. Furthermore, it was inferred that radial anisotropy predicted with typical laboratory-derived parameters exceeds tomographic observations. Here, we argue that due to finite-frequency effects and

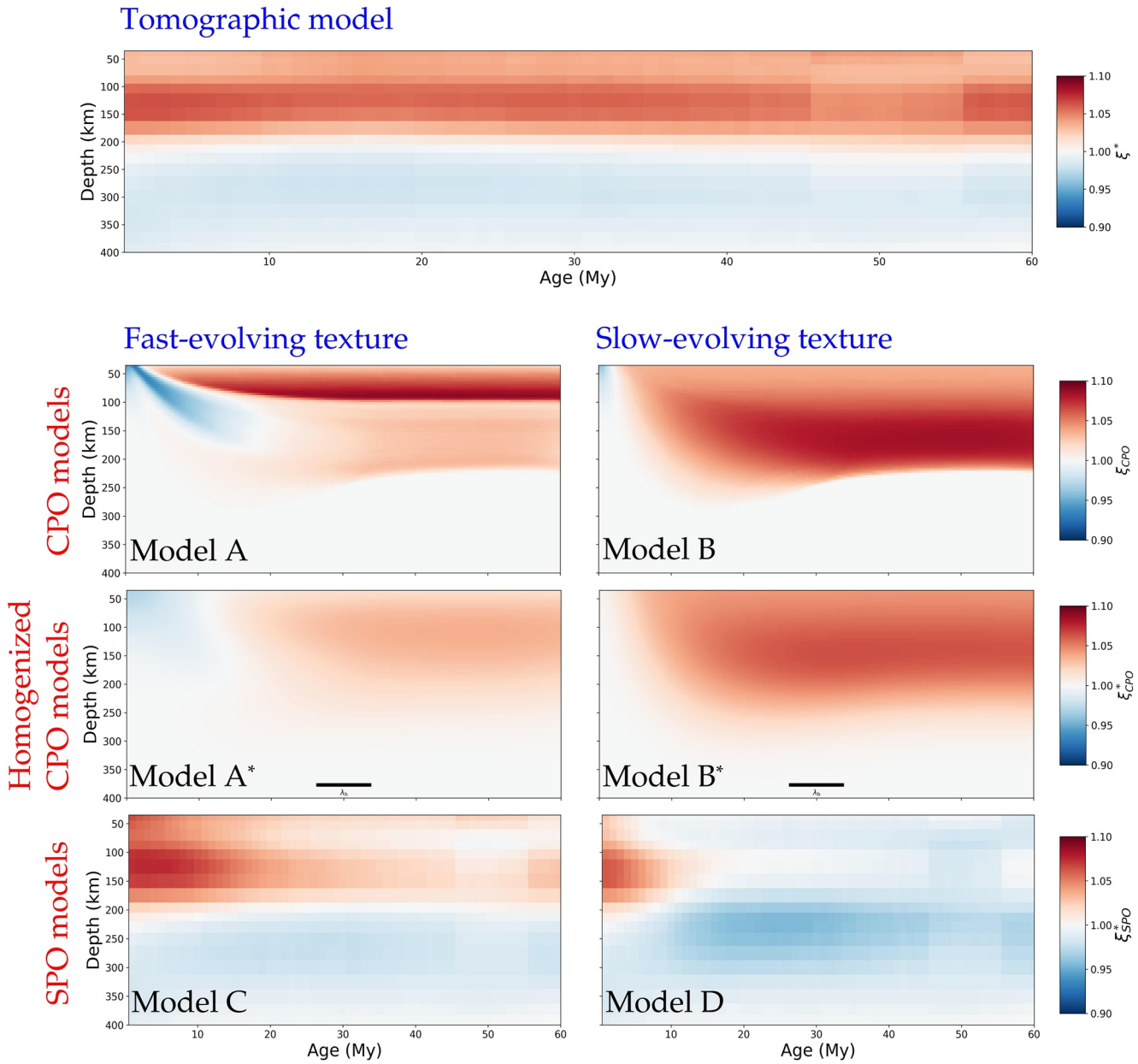

Figure 9. Plate-averaged radial anisotropy across the upper-mantle beneath oceanic basins with ages ranging between 0 and 80 Myr obtained from a tomographic model (top panel), reference CPO models corresponding to fast and slow-evolving textures (models A and B), homogenized versions of model A (model A*) and of model B (model B*). The sudden discoloration centered at 50 My in the tomographic model may have resulted from the independent inversions for V_{SH} and V_{SV}. This artifact may be eliminated by jointly inverting Love and Rayleigh waveforms for the radial anisotropy instead. Models C and D, respectively, are the extrinsic radial anisotropy profiles computed by dividing ξ^* of the tomographic model, by ξ^*_{CPO} of model A* and B*, using the composite law. Positive lithospheric radial anisotropy in model C implies the existence of horizontally laminated structures. This is absent in model D which is expected since model B* is designed to fit observations.

eventually limitations in resolution power, seismic tomography instead may underestimate the strength of intrinsic anisotropy, which further reinforce the need for the presence of a non-negligible SPO. As opposed to common practice, the physical parameters used in CPO models of which are initially constrained by experimental data may need not be manually tuned, and perhaps that the action of varying such parameters to conform with tomographic observations deems unnecessary. We therefore conclude that direct visual comparison between a CPO model and a tomographic model could lead to wrong interpretations, and that homogenization is necessary to have correct interpretations of the CPO models.

6.4. Deriving an SPO Model

The SPO models of Figure 9 (models C and D) can be estimated by using our composite law in Equation 28. The extrinsic radial anisotropy is obtained by simply dividing the tomographic model of radial anisotropy by that of the homogenized CPO model:

$$\xi^*_{\mathrm{SPO}} = \frac{\xi^*}{\xi^*_{\mathrm{CPO}}}. \tag{34}$$

In this way, models C and D are obtained from models A^* and B^*, respectively.

Strong levels of positive extrinsic radial anisotropy near the ridge axis may be due to the inability of surface waves to register vertical flow because of its limited lateral resolution. Model D, associated with the slow-evolving CPO model B, is almost devoid of SPO. This is expected since model B was tailored to fit seismic tomography observations from CPO only. Based on our results, one should favor SPO model C that corresponds to a fast-evolving CPO model. It displays positive extrinsic radial anisotropy above 200 km depth. This is more consistent with the existence of lateral fine-scale structures at the base of the lithosphere (e.g., Auer et al., 2015; Kennett & Furumura, 2015). In contradiction with previous findings, the fast mobility model becomes acceptable when a conservative estimate of tomography resolution is obtained by homogenization and a significant part of radial anisotropy under oceanic plate is due to SPO.

7. Conclusion

Differentiating the relative contributions of CPO and SPO to the full effective medium is not a simple, straightforward process. The tomographic operator (here approximated by $\mathcal{H}$) acts as a smoothing operator, and its inverse is highly non-unique. It is therefore clearly impossible to separate the CPO and SPO contributions in a tomographic model. One of the most logical courses of action is to compare tomographic models of anisotropy with existing micro-mechanical models of CPO evolution (e.g., Becker et al., 2003, 2006; Ferreira et al., 2019). Here, we proposed an approximated composite law that directly relates the separate contributions of CPO and SPO to the full effective radial anisotropy ξ^* inferred from tomographic models:

$$\xi^* \approx \xi^*_{\mathrm{SPO}} \times \xi^*_{\mathrm{CPO}},$$

which we have numerically verified using simple 2-D toy models of an intrinsically anisotropic and a heterogeneous mantle. Although our numerical experiments were mainly a proof-of-concept, comparing a CPO model directly to an existing tomographic model is unwarranted and we highly recommend homogenizing a CPO model as an intermediate step.

Data Availability Statement

The texture evolution modeling software, D-Rex (Kaminski et al., 2004), is available at http://www.ipgp.fr/~kaminski/web_doudoud/DRex.tar.gz. At the moment, the Fast Fourier Homogenization (FFH) software is only available upon request to Yann Capdeville. Author details can be found in https://lpg-umr6112.fr/index.php?option=com_content&view=article&id=594&lang=en. The FFH algorithm is described comprehensively in the following in-text citation references: Capdeville et al. (2015) and Capdeville and Métivier (2018). This study is entirely theoretical. No data have been used or produced for this study.

Acknowledgments
This study has been funded by the European Union Horizon 2020 research and innovation program under grant agreement 716542. The computations were performed through the in-house TRANSCALE cluster situated in Lyon. The authors would like to thank editor Michael Bostock, an anonymous associate editor, and two anonymous reviewers for the constructive review.

References

Agranier, A., Blichert-Toft, J., Graham, D., Debaille, V., Schiano, P., & Albarède, F. (2005). The spectra of isotopic heterogeneities along the mid-atlantic ridge. *Earth and Planetary Science Letters*, *238*(1–2), 96–109. https://doi.org/10.1016/j.epsl.2005.07.011

Alder, C., Bodin, T., Ricard, Y., Capdeville, Y., Debayle, E., & Montagner, J. (2017). Quantifying seismic anisotropy induced by small-scale chemical heterogeneities. *Geophysical Journal International*, *211*(3), 1585–1600. https://doi.org/10.1093/gji/ggx389

Allègre, C. J., & Turcotte, D. L. (1986). Implications of a two-component marble-cake mantle. *Nature*, *323*(6084), 123–127. https://doi.org/10.1038/323123a0

Auer, L., Becker, T. W., Boschi, L., & Schmerr, N. (2015). Thermal structure, radial anisotropy, and dynamics of oceanic boundary layers. *Geophysical Research Letters*, *42*(22), 9740–9749. https://doi.org/10.1002/2015gl066246

Backus, G. E. (1962). Long-wave elastic anisotropy produced by horizontal layering. *Journal of Geophysical Research*, *67*(11), 4427–4440. https://doi.org/10.1029/jz067i011p04427

Bakulin, A. (2003). Intrinsic and layer-induced vertical transverse isotropy. *Geophysics*, *68*(5), 1708–1713. https://doi.org/10.1190/1.1620644

Ballmer, M. D., Schmerr, N. C., Nakagawa, T., & Ritsema, J. (2015). Compositional mantle layering revealed by slab stagnation at ~1000-km depth. *Science Advances*, *1*(11), e1500815. https://doi.org/10.1126/sciadv.1500815
Becker, T. W., Chevrot, S., Schulte-Pelkum, V., & Blackman, D. K. (2006). Statistical properties of seismic anisotropy predicted by upper mantle geodynamic models. *Journal of Geophysical Research: Solid Earth*, *111*(B8). https://doi.org/10.1029/2005jb004095
Becker, T. W., Kellogg, J. B., Ekström, G., & O'Connell, R. J. (2003). Comparison of azimuthal seismic anisotropy from surface waves and finite strain from global mantle-circulation models. *Geophysical Journal International*, *155*(2), 696–714. https://doi.org/10.1046/j.1365-246x.2003.02085.x
Becker, T. W., Kustowski, B., & Ekström, G. (2008). Radial seismic anisotropy as a constraint for upper mantle rheology. *Earth and Planetary Science Letters*, *267*(1–2), 213–227. https://doi.org/10.1016/j.epsl.2007.11.038
Beghein, C., Snoke, J. A., & Fouch, M. J. (2010). Depth constraints on azimuthal anisotropy in the great basin from Rayleigh-wave phase velocity maps. *Earth and Planetary Science Letters*, *289*(3–4), 467–478. https://doi.org/10.1016/j.epsl.2009.11.036
Beghein, C., Trampert, J., & Van Heijst, H. (2006). Radial anisotropy in seismic reference models of the mantle. *Journal of Geophysical Research: Solid Earth*, *111*(B2). https://doi.org/10.1029/2005jb003728
Beghein, C., Xing, Z., & Goes, S. (2019). Thermal nature and resolution of the lithosphere–asthenosphere boundary under the Pacific from surface waves. *Geophysical Journal International*, *216*(2), 1441–1465. https://doi.org/10.1093/gji/ggy490
Bodin, T., Capdeville, Y., Romanowicz, B., & Montagner, J. P. (2015). Interpreting radial anisotropy in global and regional tomographic models. In *The Earth's heterogeneous mantle* (pp. 105–144). Springer. https://doi.org/10.1007/978-3-319-15627-9_4
Boneh, Y., Morales, L. F., Kaminski, E., & Skemer, P. (2015). Modeling olivine CPO evolution with complex deformation histories: Implications for the interpretation of seismic anisotropy in the mantle. *Geochemistry, Geophysics, Geosystems*, *16*(10), 3436–3455. https://doi.org/10.1002/2015gc005964
Browaeys, J. T., & Chevrot, S. (2004). Decomposition of the elastic tensor and geophysical applications. *Geophysical Journal International*, *159*(2), 667–678. https://doi.org/10.1111/j.1365-246x.2004.02415.x
Burgos, G., Montagner, J.-P., Beucler, E., Capdeville, Y., Mocquet, A., & Drilleau, M. (2014). Oceanic lithosphere-asthenosphere boundary from surface wave dispersion data. *Journal of Geophysical Research: Solid Earth*, *119*(2), 1079–1093. https://doi.org/10.1002/2013jb010528
Bystricky, M., Kunze, K., Burlini, L., & Burg, J.-P. (2000). High shear strain of olivine aggregates: Rheological and seismic consequences. *Science*, *290*(5496), 1564–1567. https://doi.org/10.1126/science.290.5496.1564
Capdeville, Y., Guillot, L., & Marigo, J.-J. (2010). 2-D non-periodic homogenization to upscale elastic media for P–SV waves. *Geophysical Journal International*, *182*(2), 903–922. https://doi.org/10.1111/j.1365-246x.2010.04636.x
Capdeville, Y., & Marigo, J.-J. (2007). Second order homogenization of the elastic wave equation for non-periodic layered media. *Geophysical Journal International*, *170*(2), 823–838. https://doi.org/10.1111/j.1365-246x.2007.03462.x
Capdeville, Y., & Métivier, L. (2018). Elastic full waveform inversion based on the homogenization method: Theoretical framework and 2-D numerical illustrations. *Geophysical Journal International*, *213*(2), 1093–1112. https://doi.org/10.1093/gji/ggy039
Capdeville, Y., Stutzmann, E., Wang, N., & Montagner, J. P. (2013). Residual homogenization for seismic forward and inverse problems in layered media. *Geophysical Journal International*, *194*(1), 470–487. https://doi.org/10.1093/gji/ggt102
Capdeville, Y., Zhao, M., & Cupillard, P. (2015). Fast Fourier homogenization for elastic wave propagation in complex media. *Wave Motion*, *54*, 170–186. https://doi.org/10.1016/j.wavemoti.2014.12.006
Chang, S.-J., & Ferreira, A. M. (2019). Inference on water content in the mantle transition zone near subducted slabs from anisotropy tomography. *Geochemistry, Geophysics, Geosystems*, *20*(2), 1189–1201. https://doi.org/10.1029/2018gc008090
Chen, W.-P., & Brudzinski, M. R. (2003). Seismic anisotropy in the mantle transition zone beneath Fiji-Tonga. *Geophysical Research Letters*, *30*(13). https://doi.org/10.1029/2002gl016330
Coltice, N., & Ricard, Y. (1999). Geochemical observations and one layer mantle convection. *Earth and Planetary Science Letters*, *174*(1–2), 125–137. https://doi.org/10.1016/s0012-821x(99)00258-7
Connolly, J. A. (2005). Computation of phase equilibria by linear programming: A tool for geodynamic modeling and its application to subduction zone decarbonation. *Earth and Planetary Science Letters*, *236*(1–2), 524–541. https://doi.org/10.1016/j.epsl.2005.04.033
Connolly, J. A. (2009). The geodynamic equation of state: What and how. *Geochemistry, Geophysics, Geosystems*, *10*(10). https://doi.org/10.1029/2009gc002540
Cowin, S. C., & Mehrabadi, M. M. (1987). On the identification of material symmetry for anisotropic elastic materials. *Quarterly Journal of Mechanics & Applied Mathematics*, *40*(4), 451–476. https://doi.org/10.1093/qjmam/40.4.451
Crampin, S., & Booth, D. C. (1985). Shear-wave polarizations near the north Anatolian fault—II. Interpretation in terms of crack-induced anisotropy. *Geophysical Journal International*, *83*(1), 75–92. https://doi.org/10.1111/j.1365-246x.1985.tb05157.x
Davies, D. R., Wilson, C. R., & Kramer, S. C. (2011). Fluidity: A fully unstructured anisotropic adaptive mesh computational modeling framework for geodynamics. *Geochemistry, Geophysics, Geosystems*, *12*(6). https://doi.org/10.1029/2011gc003551
Debayle, E. (1999). Sv-wave azimuthal anisotropy in the Australian upper mantle: Preliminary results from automated Rayleigh waveform inversion. *Geophysical Journal International*, *137*(3), 747–754. https://doi.org/10.1046/j.1365-246x.1999.00832.x
Debayle, E., Bodin, T., Durand, S., & Ricard, Y. (2020). Seismic evidence for partial melt below tectonic plates. *Nature*, *586*(7830), 555–559. https://doi.org/10.1038/s41586-020-2809-4
Debayle, E., & Kennett, B. (2000). Anisotropy in the Australasian upper mantle from love and Rayleigh waveform inversion. *Earth and Planetary Science Letters*, *184*(1), 339–351. https://doi.org/10.1016/s0012-821x(00)00314-9
Debayle, E., & Ricard, Y. (2012). A global shear velocity model of the upper mantle from fundamental and higher Rayleigh mode measurements. *Journal of Geophysical Research: Solid Earth*, *117*(B10). https://doi.org/10.1029/2012jb009288
Debayle, E., & Ricard, Y. (2013). Seismic observations of large-scale deformation at the bottom of fast-moving plates. *Earth and Planetary Science Letters*, *376*, 165–177. https://doi.org/10.1016/j.epsl.2013.06.025
Ekström, G., & Dziewonski, A. M. (1998). The unique anisotropy of the Pacific upper mantle. *Nature*, *394*(6689), 168–172. https://doi.org/10.1038/28148
Estey, L. H., & Douglas, B. J. (1986). Upper mantle anisotropy: A preliminary model. *Journal of Geophysical Research: Solid Earth*, *91*(B11), 11393–11406. https://doi.org/10.1029/jb091ib11p11393
Faccenda, M., Ferreira, A. M., Tisato, N., Lithgow-Bertelloni, C., Stixrude, L., & Pennacchioni, G. (2019). Extrinsic elastic anisotropy in a compositionally heterogeneous Earth's mantle. *Journal of Geophysical Research: Solid Earth*, *124*(2), 1671–1687. https://doi.org/10.1029/2018jb016482
Ferreira, A. M., Faccenda, M., Sturgeon, W., Chang, S.-J., & Schardong, L. (2019). Ubiquitous lower-mantle anisotropy beneath subduction zones. *Nature Geoscience*, *12*(4), 301–306. https://doi.org/10.1038/s41561-019-0325-7

Fichtner, A., Kennett, B. L., Igel, H., & Bunge, H.-P. (2010). Full waveform tomography for radially anisotropic structure: New insights into present and past states of the Australasian upper mantle. *Earth and Planetary Science Letters*, *290*(3–4), 270–280. https://doi.org/10.1016/j.epsl.2009.12.003

Fichtner, A., Kennett, B. L., & Trampert, J. (2013). Separating intrinsic and apparent anisotropy. *Physics of the Earth and Planetary Interiors*, *219*, 11–20. https://doi.org/10.1016/j.pepi.2013.03.006

French, S., Lekic, V., & Romanowicz, B. (2013). Waveform tomography reveals channeled flow at the base of the oceanic asthenosphere. *Science*, *342*(6155), 227–230. https://doi.org/10.1126/science.1241514

Friederich, W., & Huang, Z.-X. (1996). Evidence for upper mantle anisotropy beneath southern Germany from love and Rayleigh wave dispersion. *Geophysical Research Letters*, *23*(10), 1135–1138. https://doi.org/10.1029/96gl01216

Garel, F., Goes, S., Davies, D., Davies, J. H., Kramer, S. C., & Wilson, C. R. (2014). Interaction of subducted slabs with the mantle transition-zone: A regime diagram from 2-D thermo-mechanical models with a mobile trench and an overriding plate. *Geochemistry, Geophysics, Geosystems*, *15*(5), 1739–1765. https://doi.org/10.1002/2014gc005257

Guillot, L., Capdeville, Y., & Marigo, J.-J. (2010). 2-D non-periodic homogenization of the elastic wave equation: Sh case. *Geophysical Journal International*, *182*(3), 1438–1454. https://doi.org/10.1111/j.1365-246x.2010.04688.x

Gung, Y., Panning, M., & Romanowicz, B. (2003). Global anisotropy and the thickness of continents. *Nature*, *422*(6933), 707–711. https://doi.org/10.1038/nature01559

Hacker, B. R., Abers, G. A., & Peacock, S. M. (2003). Subduction factory 1. Theoretical mineralogy, densities, seismic wave speeds, and H_2O contents. *Journal of Geophysical Research: Solid Earth*, *108*(B1). https://doi.org/10.1029/2001jb001127

Hansen, L. N., Faccenda, M., & Warren, J. M. (2021). A review of mechanisms generating seismic anisotropy in the upper mantle. *Physics of the Earth and Planetary Interiors*, *313*, 106662. https://doi.org/10.1016/j.pepi.2021.106662

Hansen, L. N., Qi, C., & Warren, J. M. (2016). Olivine anisotropy suggests Gutenberg discontinuity is not the base of the lithosphere. *Proceedings of the National Academy of Sciences of the United States of America*, *113*(38), 10503–10506. https://doi.org/10.1073/pnas.1608269113

Hedjazian, N., Capdeville, Y., & Thomas, B. (2021). Multiscale seismic imaging with inverse homogenization. *Geophysical Journal International*. *226*(1), 676–691. https://doi.org/10.1093/gji/ggab121

Hedjazian, N., Garel, F., Davies, D. R., & Kaminski, E. (2017). Age-independent seismic anisotropy under oceanic plates explained by strain history in the asthenosphere. *Earth and Planetary Science Letters*, *460*, 135–142. https://doi.org/10.1016/j.epsl.2016.12.004

Ho, T., Priestley, K., & Debayle, E. (2016). A global horizontal shear velocity model of the upper mantle from multimode love wave measurements. *Geophysical Journal International*, *207*(1), 542–561. https://doi.org/10.1093/gji/ggw292

Hofmann, A. W. (1988). Chemical differentiation of the Earth: The relationship between mantle, continental crust, and oceanic crust. *Earth and Planetary Science Letters*, *90*(3), 297–314. https://doi.org/10.1016/0012-821x(88)90132-x

Kaminski, É., & Ribe, N. M. (2002). Timescales for the evolution of seismic anisotropy in mantle flow. *Geochemistry, Geophysics, Geosystems*, *3*(8), 1–17. https://doi.org/10.1029/2001gc000222

Kaminski, É., Ribe, N. M., & Browaeys, J. T. (2004). D-Rex, a program for calculation of seismic anisotropy due to crystal lattice preferred orientation in the convective upper mantle. *Geophysical Journal International*, *158*(2), 744–752. https://doi.org/10.1111/j.1365-246x.2004.02308.x

Kawakatsu, H., Kumar, P., Takei, Y., Shinohara, M., Kanazawa, T., Araki, E., & Suyehiro, K. (2009). Seismic evidence for sharp lithosphere-asthenosphere boundaries of oceanic plates. *Science*, *324*(5926), 499–502. https://doi.org/10.1126/science.1169499

Kendall, J. (2000). Seismic anisotropy in the boundary layers of the mantle. *Earth's Deep Interior: Mineral Physics and Tomography from the Atomic to the Global Scale*, *117*, 133–159. https://doi.org/10.1029/gm117p0133

Kendall, J., & Silver, P. (1998). Investigating causes of D″ anisotropy. *The Core-Mantle Boundary Region*, *28*, 97–118. https://doi.org/10.1029/gd028p0097

Kennett, B., & Furumura, T. (2015). Toward the reconciliation of seismological and petrological perspectives on oceanic lithosphere heterogeneity. *Geochemistry, Geophysics, Geosystems*, *16*(9), 3129–3141. https://doi.org/10.1002/2015gc006017

Koelemeijer, P., Ritsema, J., Deuss, A., & Van Heijst, H.-J. (2016). SP12RTS: A degree-12 model of shear-and compressional-wave velocity for Earth's mantle. *Geophysical Journal International*, *204*(2), 1024–1039. https://doi.org/10.1093/gji/ggv481

Kumazawa, M., & Anderson, O. L. (1969). Elastic moduli, pressure derivatives, and temperature derivatives of single-crystal olivine and single-crystal forsterite. *Journal of Geophysical Research*, *74*(25), 5961–5972. https://doi.org/10.1029/jb074i025p05961

Lev, E., & Hager, B. H. (2008). Prediction of anisotropy from flow models: A comparison of three methods. *Geochemistry, Geophysics, Geosystems*, *9*(7). https://doi.org/10.1029/2008gc002032

Long, M. D. (2013). Constraints on subduction geodynamics from seismic anisotropy. *Reviews of Geophysics*, *51*(1), 76–112. https://doi.org/10.1002/rog.20008

Long, M. D., & Becker, T. W. (2010). Mantle dynamics and seismic anisotropy. *Earth and Planetary Science Letters*, *297*(3–4), 341–354. https://doi.org/10.1016/j.epsl.2010.06.036

Love, A. E. H. (1906). *A treatise on the mathematical theory of elasticity*. The University Press.

Mancinelli, N., Shearer, P., & Liu, Q. (2016). Constraints on the heterogeneity spectrum of Earth's upper mantle. *Journal of Geophysical Research: Solid Earth*, *121*(5), 3703–3721. https://doi.org/10.1002/2015jb012641

Masters, G., Johnson, S., Laske, G., & Bolton, H. (1996). A shear-velocity model of the mantle. *Philosophical Transactions of the Royal Society of London,Series A: Mathematical, Physical and Engineering Sciences*, *354*(1711), 1385–1411.

Masters, G., Laske, G., Bolton, H., & Dziewonski, A. (2000). The relative behavior of shear velocity, bulk sound speed, and compressional velocity in the mantle: Implications for chemical and thermal structure. *Earth's Deep Interior: Mineral Physics and Tomography from the Atomic to the Global Scale*, *117*, 63–87. https://doi.org/10.1029/gm117p0063

Maupin, V., & Park, J. (2015). 1.09—Theory and observations—Seismic anisotropy. *Treatise on Geophysics*, 277–305. https://doi.org/10.1016/b978-0-444-53802-4.00007-5

Maupin, V., Park, J., Romanowicz, B., & Dziewonski, A. (2007). Theory and observations—Wave propagation in anisotropic media. Seismology and the structure of the Earth. *Treatise on Geophysics*, *1*, 289–321. https://doi.org/10.1016/b978-044452748-6/00007-9

McKenzie, D. (1979). Finite deformation during fluid flow. *Geophysical Journal International*, *58*(3), 689–715. https://doi.org/10.1111/j.1365-246x.1979.tb04803.x

McNamara, A. K., van Keken, P. E., & Karato, S. (2002). Development of anisotropic structure by solid-state convection in the Earth's lower mantle. *Nature*, *416*(6878), 310–314. https://doi.org/10.1038/416310a

Meade, C., Silver, P. G., & Kaneshima, S. (1995). Laboratory and seismological observations of lower mantle isotropy. *Geophysical Research Letters*, *22*(10), 1293–1296. https://doi.org/10.1029/95gl01091

Montagner, J. P. (1985). Seismic anisotropy of the Pacific Ocean inferred from long-period surface waves dispersion. *Physics of the Earth and Planetary Interiors*, *38*(1), 28–50. https://doi.org/10.1016/0031-9201(85)90120-7

Montagner, J. P. (2007). Upper mantle structure: Global isotropic and anisotropic elastic tomography. *Treatise on Geophysics*, *1*, 559–589. https://doi.org/10.1016/b978-044452748-6.00018-3

Montagner, J.-P., & Jobert, N. (1988). Vectorial tomography—II. Application to the Indian Ocean. *Geophysical Journal International*, *94*(2), 309–344. https://doi.org/10.1111/j.1365-246x.1988.tb05904.x

Montagner, J. P., & Nataf, H.-C. (1986). A simple method for inverting the azimuthal anisotropy of surface waves. *Journal of Geophysical Research: Solid Earth*, *91*(B1), 511–520. https://doi.org/10.1029/jb091ib01p00511

Montagner, J. P., & Nataf, H.-C. (1988). Vectorial tomography. Part I: Theory. *Geophysical Journal International*, *94*, 295–307. https://doi.org/10.1111/j.1365-246x.1988.tb05903.x

Moulinec, H., & Suquet, P. (1998). A numerical method for computing the overall response of nonlinear composites with complex microstructure. *Computer Methods in Applied Mechanics and Engineering*, *157*(1), 69–94. https://doi.org/10.1016/s0045-7825(97)00218-1

Nettles, M., & Dziewoński, A. M. (2008). Radially anisotropic shear velocity structure of the upper mantle globally and beneath North America. *Journal of Geophysical Research: Solid Earth*, *113*(B2). https://doi.org/10.1029/2006jb004819

Nicolas, A., Boudier, F., & Boullier, A. (1973). Mechanisms of flow in naturally and experimentally deformed peridotites. *American Journal of Science*, *273*(10), 853–876. https://doi.org/10.2475/ajs.273.10.853

Nicolas, A., & Christensen, N. I. (1987). Formation of anisotropy in upper mantle peridotites—A review. *Composition, Structure and Dynamics of the Lithosphere-Asthenosphere System*, *16*, 111–123. https://doi.org/10.1029/gd016p0111

Obrebski, M., Kiselev, S., Vinnik, L., & Montagner, J.-P. (2010). Anisotropic stratification beneath Africa from joint inversion of SKS and P receiver functions. *Journal of Geophysical Research: Solid Earth*, *115*(B9). https://doi.org/10.1029/2009jb006923

Panning, M., & Romanowicz, B. (2006). A three-dimensional radially anisotropic model of shear velocity in the whole mantle. *Geophysical Journal International*, *167*(1), 361–379. https://doi.org/10.1111/j.1365-246x.2006.03100.x

Plomerová, J., Kouba, D., & Babuška, V. (2002). Mapping the lithosphere–asthenosphere boundary through changes in surface-wave anisotropy. *Tectonophysics*, *358*(1–4), 175–185. https://doi.org/10.1016/s0040-1951(02)00423-7

Press, W. H., Teukolsky, S. A., Flannery, B. P., & Vetterling, W. T. (1992). *Numerical recipes in Fortran 77: Volume 1 of Fortran numerical recipes: The art of scientific computing*. Cambridge University Press.

Resovsky, J. S., & Ritzwoller, M. H. (1999). A degree 8 mantle shear velocity model from normal mode observations below 3 mHz. *Journal of Geophysical Research: Solid Earth*, *104*(B1), 993–1014. https://doi.org/10.1029/1998jb900025

Ricard, Y., & Bercovici, D. (2009). A continuum theory of grain size evolution and damage. *Journal of Geophysical Research: Solid Earth*, *114*(B1). https://doi.org/10.1029/2007jb005491

Ricard, Y., Durand, S., Montagner, J.-P., & Chambat, F. (2014). Is there seismic attenuation in the mantle? *Earth and Planetary Science Letters*, *388*, 257–264. https://doi.org/10.1016/j.epsl.2013.12.008

Rychert, C. A., Harmon, N., & Tharimena, S. (2018). Seismic imaging of the base of the ocean plates. In *Lithospheric discontinuities* (pp. 71–87). American Geophysical Union. https://doi.org/10.1002/9781119249740.ch4

Rychert, C. A., & Shearer, P. M. (2011). Imaging the lithosphere-asthenosphere boundary beneath the pacific using SS waveform modeling. *Journal of Geophysical Research: Solid Earth*, *116*(B7). https://doi.org/10.1029/2010jb008070

Sanchez-Palencia, E. (1980). *Non homogeneous media and vibration theory (No. 27)*. Springer.

Schlue, J., & Knopoff, L. (1977). Shear-wave polarization anisotropy in the pacific basin. *Geophysical Journal International*, *49*(1), 145–165. https://doi.org/10.1111/j.1365-246x.1977.tb03706.x

Simmons, N. A., Schuberth, B. S., Myers, S. C., & Knapp, D. R. (2019). Resolution and covariance of the LLNL-G3D-JPS global seismic tomography model: Applications to travel time uncertainty and tomographic filtering of geodynamic models. *Geophysical Journal International*, *217*(3), 1543–1557. https://doi.org/10.1093/gji/ggz102

Stixrude, L., & Jeanloz, R. (2015). *Constraints on seismic models from other disciplines-constraints from mineral physics on seismological models*.

Stixrude, L., & Lithgow-Bertelloni, C. (2011). Thermodynamics of mantle minerals—II. Phase equilibria. *Geophysical Journal International*, *184*(3), 1180–1213. https://doi.org/10.1111/j.1365-246x.2010.04890.x

Sturgeon, W., Ferreira, A. M., Faccenda, M., Chang, S.-J., & Schardong, L. (2019). On the origin of radial anisotropy near subducted slabs in the midmantle. *Geochemistry, Geophysics, Geosystems*, *20*(11), 5105–5125. https://doi.org/10.1029/2019gc008462

Takeuchi, H., & Saito, M. (1972). Seismic surface waves. *Methods in Computational Physics*, *11*, 217–295. https://doi.org/10.1016/b978-0-12-460811-5.50010-6

Tauzin, B., Bodin, T., Debayle, E., Perrillat, J.-P., & Reynard, B. (2016). Multi-mode conversion imaging of the subducted Gorda and Juan de fuca plates below the north American continent. *Earth and Planetary Science Letters*, *440*, 135–146. https://doi.org/10.1016/j.epsl.2016.01.036

Tauzin, B., & Ricard, Y. (2014). Seismically deduced thermodynamics phase diagrams for the mantle transition zone. *Earth and Planetary Science Letters*, *401*, 337–346. https://doi.org/10.1016/j.epsl.2014.05.039

Thomsen, L. (1986). Weak elastic anisotropy. *Geophysics*, *51*(10), 1954–1966. https://doi.org/10.1190/1.1442051

Tkalčić, H., Pasyanos, M. E., Rodgers, A. J., Gök, R., Walter, W., & Al-Amri, A. (2006). A multistep approach for joint modeling of surface wave dispersion and teleseismic receiver functions: Implications for lithospheric structure of the Arabian Peninsula. *Journal of Geophysical Research: Solid Earth*, *111*(B11).

Tommasi, A., Mainprice, D., Canova, G., & Chastel, Y. (2000). Viscoplastic self-consistent and equilibrium-based modeling of olivine lattice preferred orientations: Implications for the upper mantle seismic anisotropy. *Journal of Geophysical Research: Solid Earth*, *105*(B4), 7893–7908. https://doi.org/10.1029/1999jb900411

Trampert, J., & van Heijst, H. J. (2002). Global azimuthal anisotropy in the transition zone. *Science*, *296*(5571), 1297–1299. https://doi.org/10.1126/science.1070264

Wang, N., Montagner, J. P., Fichtner, A., & Capdeville, Y. (2013). Intrinsic versus extrinsic seismic anisotropy: The radial anisotropy in reference Earth models. *Geophysical Research Letters*, *40*(16), 4284–4288. https://doi.org/10.1002/grl.50873

Wookey, J., & Kendall, J.-M. (2004). Evidence of midmantle anisotropy from shear wave splitting and the influence of shear-coupled P waves. *Journal of Geophysical Research: Solid Earth*, *109*(B7). https://doi.org/10.1029/2003jb002871

Xie, J., Ritzwoller, M. H., Shen, W., & Wang, W. (2017). Crustal anisotropy across eastern Tibet and surroundings modeled as a depth-dependent tilted hexagonally symmetric medium. *Geophysical Journal International*, *209*(1), 466–491. https://doi.org/10.1093/gji/ggx004

Xie, J., Ritzwoller, M. H., Shen, W., Yang, Y., Zheng, Y., & Zhou, L. (2013). Crustal radial anisotropy across eastern Tibet and the western Yangtze craton. *Journal of Geophysical Research: Solid Earth*, *118*(8), 4226–4252. https://doi.org/10.1002/jgrb.50296

Xu, W., Lithgow-Bertelloni, C., Stixrude, L., & Ritsema, J. (2008). The effect of bulk composition and temperature on mantle seismic structure. *Earth and Planetary Science Letters*, *275*(1–2), 70–79. https://doi.org/10.1016/j.epsl.2008.08.012

Zhang, S., & Karato, S.-i. (1995). Lattice preferred orientation of olivine aggregates deformed in simple shear. *Nature*, *375*(6534), 774–777. https://doi.org/10.1038/375774a0